CHAPTER 15

ESR AND SLOW MOTIONS IN LIQUID CRYSTALS

J. H. FREED, A. NAYEEM and S. B. RANANAVARE
Baker Laboratory of Chemistry
Cornell University
Ithaca
New York 14853
USA

ABSTRACT. The theory of slow motional ESR is outlined, with applications to nitroxide spectra in liquid crystals. The computer algorithms for implementing the theory based on the stochastic Liouville equation are also discussed.

1. Introduction

In this Chapter, the theory of slow tumbling in ESR spectroscopy is outlined, with specific application to the free radical spectra from nitroxides dissolved in liquid crystals. The slow tumbling region is that for which the ESR spectra can no longer be described as a simple superposition of three lorentzian lines, for which the motional narrowing theory developed in Chapters 12 and 13 applies. It is taken to be the region for which the ESR spectra still show motional effects, i.e., the rigid limit has not been reached. For nitroxides, this typically means that the rotational correlation times being considered lie between nanoseconds and microseconds [1,2]. (New time domain ESR methods have extended this range to the millisecond regime (cf. section 7)). This time scale is typical of motions of spin probes in viscous media, or slowly diffusing macromolecules in solution. Owing to the greater sensitivity of spectra to details of molecular motion in the slow motional regime, the latter provides better means for discriminating between models than in the motional narrowing region.

From a theoretical viewpoint, the slow motional regime is that where the stochastic perturbations to the spin hamiltonian (i.e., $| H_1(\Omega) |$ in Chapter 12) are comparable to, or greater than, the correlation time τ_R, i.e., $| H_1(\Omega) |^2 \tau_R^2 \geq 1$. Therefore, apart from motion, an interesting feature of the magnetic resonance experiment is that we can, in principle, tune in the slow motional regime by properly adjusting the magnetic field. This feature allows us to vary the relative magnitudes of some of the relevant terms in $H_1(\Omega)$ and thus to increase the sensitivity of the experiment to particular time scales of molecular motion. This idea has recently been used to extend the time scale of the slow motional ESR experiment to the range 10-100 ps, depending on the nature of the spin probe, by working at high fields (90 kG) and high frequencies (250 GHz) [3].

The theoretical formalism for the calculation of slow motional spectra is presented in section 1, where the basic ESR lineshape problem is described in terms of the stochastic Liouville equation. In section 2 a survey of the methods of solving the stochastic Liouville equation based on the Lanczos and conjugate gradients algorithms is presented. The close connection between these methods and Mori's method used in statistical mechanics, is discussed in section 3. In

G. R. Luckhurst and C. A. Veracini (eds.), The Molecular Dynamics of Liquid Crystals, 365–402.

sections 4 to 6, the applications of the slow motional formalism to experimental CW ESR results in liquid crystals is illustrated, while in section 7 the more recent applications of two dimensional techniques used for studies of slow motion are shown. Finally, section 8 discusses the treatment of data for the analysis of lineshapes in two dimensional ESR spectroscopy.

2. ESR Lineshapes: The Stochastic Liouville Equation

The breakdown of the fast motional theories can be traced to their perturbative nature. In the slow motional regime, the dynamics of the spins strongly couple to the orientational and/or positional degrees of freedom of the molecule which render perturbative treatments invalid. To proceed we must treat both the classical orientational and/or positional degrees of freedom and the quantum mechanical spin degrees of freedom on a more equal footing. Since solving the exact equations of motion for all the molecules in the sample is obviously an impossible task, some physically reasonable assumptions must be introduced to make the problem tractable.

First, we assume that the equation of motion for the density matrix, $\rho(t)$ has the same hamiltonian $\hat{H}(t)$ for all members of the ensemble and is given by the quantum mechanical Liouville equation

$$\partial\rho/\partial t = - i\left[\hat{H}(t), \rho\right], \tag{1}$$

where $\hat{H}(t)$ is given in angular frequency units. Now, we assume that the time dependence of the spin hamiltonian $\hat{H}(t)$ for a spin probe arises from interactions with its environment such that $\hat{H}(t)$ is fully determined by a complete set of random variables, Ω. [In practice, these may represent the set of Euler angles needed to describe the instantaneous orientation of a molecule fixed frame (e.g., the diffusion frame) with respect to a laboratory fixed frame (the z axis of which is traditionally chosen to lie along the static magnetic field or the mean director)]. We also assume that this time dependence of Ω is described by a stationary Markov process, so that the probability of being in a state Ω_2 at time t_2, if in state Ω_1 at time $t_1 = t_2 - \Delta t$, is independent of the value of Ω at any time earlier than t_1 and depends only on the time difference Δt and not on t_1. A stationary Markov process can be described by a differential equation

$$\partial P(\Omega,t)/\partial t = - \Gamma(\Omega)\, P(\Omega,t), \tag{2}$$

where $P(\Omega,t)$ is the probability of the spin probe being in a state Ω at time t.

Since the process is assumed stationary, $\Gamma(\Omega)$ is independent of time. The stochastic evolution operator $\Gamma(\Omega)$ operates only on the random variables Ω and is independent of the spin degrees of freedom. It may include such general Markov operators as the diffusion operators given by Fokker-Planck equations and matrices of transition rates among discrete states. In most of our examples, Ω will represent Euler angles specifying orientation and $\Gamma(\Omega)$ will be a rotational diffusion or Fokker-Planck operator. As noted in Chapter 4, section 1, for rotational diffusion in liquid crystals, Γ ($\equiv \Gamma_{LC}$) depends not only on the orientation of the diffusing molecule (spin probe) relative to the mean director, but it also depends on the strength of the orienting potential $U(\Omega)$ (cf. equation (1) in Chapter 4). It is given by

$$\Gamma_{LC} = \left[\mathbf{J} - \frac{1}{2k_B T}(\mathbf{J}U)\right] . \mathbf{D}_R . \left[\mathbf{J} + \frac{1}{2k_B T}(\mathbf{J}U)\right], \tag{3}$$

where the quantities in this equation have been defined previously (see Chapter 4). It is also assumed that the stochastic process has a unique equilibrium distribution $P(\Omega)$ characterised by

$$\Gamma(\Omega)\, P(\Omega) = 0. \tag{4}$$

For liquid crystals, this equilibrium distribution is given by

$$P(\Omega) = \exp\left[-\, U(\Omega)/k_B T\right] \Big/ \int d\Omega \, \exp\left[-\, U(\Omega)/k_B T\right] \tag{5}$$

which is the same as equation (13) in Chapter 4. Note that while typically only the $L = 2$ terms in the expansion for $U(\Omega)$ are kept in the expansion in terms of spherical harmonics (see Chapter 4), higher order terms have also been included in certain cases (see section E). We can even allow for dynamic cooperativity by letting $U(\Omega) \rightarrow U(t)$ such that the probe reorients in the instantaneous potential field of the surroundings. This approach is used for SRLS and for coupling to hydrodynamic and critical modes [4]. In smectic phases, the orientational potential felt by a molecular probe should depend upon the probe location within the smectic layer in order to be consistent with the observation of reduced ordering for some probes as they are expelled into alkyl chain regions (see later). Thus, the probe will experience a coupled orientation-position potential as it diffuses in the spatially non-uniform smectic ([5]) (see also Chapter 4).

It can be shown that equations (1), (2) and (4) lead to the stochastic Liouville equation of motion [1,2],

$$\begin{aligned} \partial\rho(\Omega,t)/\partial t &= -\, i\left[\hat{H}(\Omega),\, \rho(\Omega,t)\right] - \Gamma(\Omega)\, \rho(\Omega,t) \\ &= -\, i\mathbf{L}(\Omega)\, \rho(\Omega,t) - \Gamma(\Omega)\, \rho(\Omega,t), \end{aligned} \tag{6}$$

where $\rho(\Omega,t)$ is now understood to be the quantum mechanical spin density matrix and also the classical probability distribution function in molecular orientation, and $\mathbf{L}$ is the hamiltonian superoperator, or the Liouville operator. Thus, instead of looking at the explicit time dependence of the spin hamiltonian $\hat{H}(t)$ involving the interaction with its environment, the spin hamiltonian is written in terms of random variables Ω, and its modulation (e.g., $\hat{H}(t)$ due to rotational motions) is expressed by the stochastic time dependence of Ω.

In summary, the fundamental problem in slow motional ESR spectroscopy is to compare solutions of this stochastic Liouville operator equation with experimental spectra so as to extract the correct stochastic operator Γ and obtain the magnitude of the relevant physical parameters. We may refer to this as solving for the inverse stochastic Liouville transform (by analogy with the inverse scattering transform in the quantum mechanical theory of scattering). In practice, this is not possible, so we construct simple models for Γ_Ω such as those discussed in Chapter 4, to compare with experimental spectra.

The general linear response expression for the imaginary part of the magnetic susceptibility $\chi''(\omega)$ resulting from a very weak, linearly polarised microwave field of angular frequency ω being applied to the system [6] is

$$\chi''_{jj}(\omega) = (\omega/2Nk_B T)\int_0^\infty dt \left[\exp(i\omega t) + \exp(-i\omega t)\right] \mathrm{tr}\{\mathbf{M}_j(t)\, \mathbf{M}_j\} \tag{7}$$

which involves a trace over the macroscopic magnetisation operator M_j. Note that M, the macroscopic value of the magnetisation is related to M, its associated quantum mechanical operator by $M(t) = \mathrm{tr}\{\boldsymbol{\rho}(t)\, \mathbf{M}\}$. The oscillating field is taken along j = x, y or z. For our system of non-interacting (or weakly interacting) spin probes with a nearly isotropic g factor, we have

$$\mathrm{tr}\{\mathbf{M}_j(t)\,\mathbf{M}_j\} = N\gamma_e^2\,\mathrm{tr}\{\mathbf{S}_j(t)\,\mathbf{S}_j\} = N\gamma_e^2\,\mathrm{tr}\{\mathbf{S}_j\,\mathbf{S}_j(t)\}, \tag{8}$$

where N is the number of spins in the sample and γ_e is the magnetogyric ratio of the electron. In these equations, the trace is over orientational and spin degrees of freedom. The spin operator $S_j(t)$ in the Heisenberg representation obeys a stochastic Liouville equation equivalent to equation (6) given by

$$\partial S_j(\Omega,t)/\partial t = i\mathbf{L}(\Omega)\,S_j(\Omega,t) - \Gamma^{\dagger}(\Omega)\,\rho(\Omega,t), \tag{9}$$

where the superscript dagger implies the hermitian adjoint operator. We now perform a classical average over the orientational degrees of freedom, and then utilise the symmetrising transformation

$$\tilde{\Gamma}(\Omega) = P^{-1/2}(\Omega)\,\Gamma(\Omega)\,P^{1/2}(\Omega), \tag{10}$$

where $P^{\pm 1/2}(\Omega)$ are regarded as operators. This leads to the symmetrised equation

$$\mathrm{tr}_s\,\overline{S_j\,S_j(\pm\omega,\Omega)} = \left\langle P^{1/2}S_j \mid \left[i(\omega\mathbf{I} - \mathbf{L}) + \tilde{\Gamma}^{\dagger}\right]^{-1} \mid P^{1/2}S_j \right\rangle, \tag{11}$$

where the trace is over spin space only, and the bar indicates the classical average. Note that $S_j(\pm\omega,\Omega)$ in this equation is the Fourier-Laplace transform of $S_j(\Omega,t)$:

$$S_j(\pm\omega,\Omega) \equiv \int_0^{\infty} dt\,\exp(\mp i\omega t)\,S_j(\Omega,t). \tag{12}$$

This transformation of equation (10) renders $\tilde{\Gamma}$ into a form which may be represented by a symmetric matrix that is, in general, complex [1,2]. The symmetrised diffusion operator $\tilde{\Gamma}(\Omega)$ will be used in the remainder of this section. The relationship between ESR spectra and the dynamics of motion of a paramagnetic molecule can then be expressed in the form

$$I(\Delta\omega) = \pi^{-1}\,\mathrm{Re}\left\langle v \mid \left[i(\Delta\omega\mathbf{I} - \mathbf{L}) + \tilde{\Gamma}^{\dagger}\right]^{-1} \mid v \right\rangle, \tag{13}$$

where $\Delta\omega$ is the sweep variable.

3. Methods of Solution: Lanczos and Conjugate Gradient Methods

Equation (13) can be rewritten as

$$I(\Delta\omega) = \pi^{-1}\,\mathrm{Re}\left\langle v \mid u(\Delta\omega)\right\rangle, \tag{14}$$

where $\mid u(\Delta\omega)\rangle$ is the solution of the equation

$$\mathbf{A}'(\Delta\omega) \mid u(\Delta\omega)\rangle = (i\Delta\omega\mathbf{I} + \mathbf{A}) \mid u(\Delta\omega)\rangle = \mid v\rangle. \tag{15}$$

The operator or matrix $\mathbf{A}$ is defined as $\mathbf{A} = \Gamma - i\mathbf{L}$. The spectrum given by equation (15) can be calculated by either solving this equation for a range of values of $\Delta\omega$ or alternatively by diagonalising $\mathbf{A}$ only once. The matrix $\mathbf{A}$ is, in general, very large and sparse. Thus, conventional methods for solving equation (15) by inversion or by diagonalising $\mathbf{A}$ prove to be too cumbersome. We soon run out of memory even on mainframe computers, and the solution requires prohibitive amounts of computer time. Accordingly, the algorithms commonly used for the calculation of slow motional spectra from the stochastic Liouville equation fall into two main

categories based on efficiency and ability to handle large sparse matrices. First are the traditional algorithms for diagonalising matrices and solving sets of coupled linear equations. Secondly, there are the various forms of the Lanczos algorithm for tridiagonalisation and the related conjugate gradients algorithm for solving sets of linear equations.

The first class of traditional methods are characterised by a variety of strengths and difficulties. These algorithms typically amount to computational overkill for the problem at hand. For instance, the Rutishauser-QR diagonalisation [7] gives the full set of eigenvectors and eigenvalues though only a small subset are important in the final spectrum. This large computational overhead and the characteristic of destroying the sparsity structure of **A** combine to make these algorithms unattractive for the present purposes. However, an important strength of this class of algorithms is their well characterised stability and reliability.

In contrast, the Lanczos algorithm and the related conjugate gradients algorithm are much better suited for the efficient calculation of slow motional magnetic resonance spectra. They are effective in handling large sparse matrices, since they do not modify the original matrix. It is, therefore, possible to take advantage of the very special sparse structure of the stochastic Liouville matrix. In addition, all of the quantities calculated in the Lanczos algorithm are used either directly in the calculation of the spectrum or are used in the next recursive step (see later). In this sense, the Lanczos algorithm represents a good approximation to the minimal amount of computation necessary to compute magnetic resonance spectra in the linear response regime.

In a more theoretical vein, it was possible to establish the close connection between the Lanczos algorithm based upon a scheme of projection operators in Hilbert space, and the Mori projection scheme in statistical mechanics (see later). Though the emphasis here will be on applications to ESR spectroscopy, the Lanczos methods described here may be regarded as appropriate for a wide range of applications in chemical physics.

3.1. THE LANCZOS ALGORITHM

The Lanczos algorithm has been developed for complex symmetric matrices, since **A** is typically of this form or else it can be transformed to this form. It is an efficient method for tridiagonalising **A** and is particularly well suited to the solution of sets of linear algebraic equations such as equation (15) which are characterised by large sparse matrices. We find that it can lead to at least an order of magnitude reduction in computation time, and it yields results to the solution of equation (13) to a high degree of accuracy [8,9]. Here we discuss the basic Lanczos algorithm as applied to hermitian and complex symmetric matrices. More sophisticated variations of the Lanczos algorithm involving selective reorthogonalisation [10] and the identification of spurious and duplicated eigenvalues [11] have been developed to circumvent known numerical instabilities. However, the basic algorithms are sufficient for most magnetic resonance calculations.

The Lanczos algorithm proceeds by recursive projections or steps which produce successively larger tridiagonal matrix approximations to the original matrix. These projections define the so-called Lanczos vectors. If N is the dimension of the matrix, and n_s the number of recursive steps needed to converge to an accurate spectrum, then in all cases studied to date $n_s \ll N$. This inequality becomes more dramatic the more complicated the problem. In this sense, the Lanczos projections rapidly seek out, from an initial finite subspace of dimension N which is spanned by the starting basis set of orthonormal vectors: $| f_j \rangle$, $j = 1,2,...,N$, a smaller subspace spanned by the Lanczos vectors (i.e., the basis vectors for the tridiagonalised form of **A**, or $\mathbf{T}_n$) written as $| \Phi_k \rangle$, $k = 1,2,...,n$. When $n = n_s$, these Lanczos vectors are a sufficient basis for accurately representing the spectrum. In this sense the algorithm constructs subspaces that progressively

approximate the optimal reduced space for the problem. These subspaces, spanned by the Lanczos vectors are the Krylov subspaces [12] generated by span of the vectors $\mathbf{A}^{k-1} \mid \upsilon \rangle$ for $k = 1,2,...,n$. Thus, the choice of $\mid \upsilon \rangle$ as the starting vector for the Lanczos algorithm biases the projections in favour of this optimal reduced space. It is easy to show that this Krylov subspace can only contain eigenvectors of **A** with a non-zero projection on $\mid \upsilon \rangle$ in exact arithmetic.

Now, consider the recursive steps of the Lanczos algorithm. First, identify the starting vector $\mid \upsilon \rangle$ as the first Lanczos vector $\mid \Phi_1 \rangle$ in accordance with the previous discussion. A Gram-Schmidt orthogonalisation on the Krylov sequence $\mathbf{A}^{k-1} \mid \upsilon \rangle$ for $k = 1,2,...,n,$, recursively generates the set of orthornormal Lanczos vectors $\mid \Phi_k \rangle$ defined as,

$$\beta_{k+1} \mid \Phi_{k+1} \rangle = (\mathbf{I} - \mathbf{P}_k)\,\mathbf{A} \mid \Phi_k \rangle, \tag{16}$$

where β_{k+1} is the normalising coefficient chosen such that

$$\langle \Phi_k \mid \Phi_k \rangle = 1 \tag{17}$$

and $\mathbf{P}_k$ is the projection operator on the Krylov subspace spanned by the previous Lanczos vectors

$$\mathbf{P}_k = \sum_{j=1}^{k} \mid \Phi_j \rangle\langle \Phi_j \mid \qquad k \le n. \tag{18}$$

Equation (16) leads to a three term recursive relation for generating the $\mid \Phi_j \rangle$ [2]

$$\beta_{k+1} \mid \Phi_{k+1} \rangle = (\mathbf{A} - \alpha_k \mathbf{I}) \mid \Phi_k \rangle - \beta_k \mid \Phi_{k-1} \rangle, \tag{19}$$

where

$$\alpha_k = \langle \Phi_k \mid \mathbf{A} \mid \Phi_k \rangle \tag{20}$$

and

$$\beta_k = \langle \Phi_k \mid \mathbf{A} \mid \Phi_{k-1} \rangle. \tag{21}$$

It may easily be shown that **A** has an $n \times n$ tridiagonal approximation, $\mathbf{T}_n$ in the basis of Lanczos vectors, i.e.,

$$\langle \Phi_k \mid \mathbf{A} \mid \Phi_j \rangle = 0 \qquad \text{if} \quad k \neq j, j \pm 1, \tag{22}$$

while equations (20) and (21) give the non-zero matrix elements. That is, given the vectors $\mid \Phi_j \rangle$ in terms of their components $q_{j,k}$ in the original basis set, $\mid f_j \rangle$, $j = 1,2,...,N$,

$$\mid \Phi_k \rangle = \sum_{j=1}^{n} q_{j,k} \mid f_j \rangle \tag{23}$$

$$q_{j,k} = \langle f_j \mid \Phi_k \rangle \tag{24}$$

then the column vectors $\mathbf{q}_k$ form the matrix $\mathbf{Q}_n$ with orthonormal columns such that $\mathbf{Q}_n^{\dagger}\,\mathbf{Q}_n = \mathbf{I}_n$ and

$$\mathbf{T}_n = \mathbf{Q}_n^{\dagger}\,\mathbf{A}\,\mathbf{Q}_n. \tag{25}$$

This is the conventional Lanczos algorithm for real symmetric matrices **A**. The substitution of hermitian conjugation for transposition in these equations gives the analogous scheme for general

hermitian matrices.

For applications such as the calculation of magnetic resonance spectra and spectral densities associated with Fokker-Planck equations, the matrix **A** is either complex symmetric or can be transformed to complex symmetric form [8,13]. Moro and Freed [8,13] have shown that it is possible to simplify problems of this type by introducing a generalised norm and scalar product. That is, first consider the general non-hermitian case. We can introduce a biorthonormal set of functions $| \Phi_j \rangle$ and $| \Phi^{j'} \rangle$ such that

$$\langle \Phi^{j'} \mid \Phi_j \rangle = \delta_{j',j} \tag{26}$$

or, alternatively, letting $\mathbf{x}_j$ and $\mathbf{x}^{j'}$ be their column vector representations,

$$(\mathbf{x}^{j'})^{\dagger} \mathbf{x}_j = \delta_{j',j}. \tag{27}$$

However, for the case of non-defective complex symmetric matrices **A**, it is possible to let

$$\mathbf{x}^j = \mathbf{x}_j^* \tag{28}$$

such that equation (27) becomes

$$\mathbf{x}_{j'}^{\dagger} \mathbf{x}_j = \delta_{j',j} \tag{29}$$

The Lanczos recursion method remains applicable with this equation defining the generalised scalar product. Note that the left hand vector is lacking the usual complex conjugation. This is referred to as rectanormalisation [2].

In general, the time required for tridiagonalisation using the Lanczos algorithm goes approximately as $n_s N(2n_E + 21)$, where n_E is the average number of non-zero matrix elements in a row of **A** [8]. This is obviously superior to the traditional methods which require $O(N^3)$ time since $n_E, n_s \ll N$.

Finally, we note that the tridiagonal form of the complex symmetric matrix $\mathbf{T}_n = \mathbf{Q}_n^{\dagger} \mathbf{A} \mathbf{Q}_n$ allows the application of very efficient diagonalisation methods [11]. The spectrum defined by equation (13) can easily be computed using the eigenvalues of $\mathbf{T}_n$ and the projections of the associated eigenvectors on the starting vector. However, for computing CW spectra, a continued fraction method [8] can be used directly on the elements of the matrix $\mathbf{T}_n$. That is, since $| \upsilon \rangle$ is the first Lanczos vector and the Lanczos vectors are orthogonal in the sense of equation (29), the spectrum is given by,

$$I(\Delta\omega) = \pi^{-1} \left(\left[i\Delta\omega \mathbf{I}_n + \mathbf{T}_n \right]^{-1} \right)_{1,1}. \tag{30}$$

By examining the structure of the (1,1) element of the inverse of successively larger principal submatrices of $[i\Delta\omega\mathbf{I}_n + \mathbf{T}_n]$ it is easy to show that the $I(\Delta\omega)$ can be written in the continued fraction form [8],

$$I(\Delta\omega) = \pi^{-1} \operatorname{Re} \left\{ \cfrac{1}{i\Delta\omega + \alpha_1 - \cfrac{\beta_1^2}{i\Delta\omega + \alpha_2 - \beta_2^2 \ldots}} \right\}. \tag{31}$$

The application of the Lanczos algorithm to **A** generates the continued fraction representation of the spectrum or spectral density. The same result, apart from the identification of $\tilde{\Gamma}$ with the

classical Liouville operator, has been derived by Mori in the context of the dynamics of systems of interacting particles [14]. The connection between the Lanczos algorithm and Mori's method is made clear in the next section.

The relation specified by the continued fraction in equation (31) is quite general. Analytical calculation of the coefficients α_j and β_j from the explicit operator form of **A** is possible and has been carried out in simple cases [15]. The axially symmetric g tensor problem is an example where this type of calculation is practical. This approach quickly leads to extremely complicated formulae which are difficult to handle for the general case. Therefore, numerical implementation of the recursive relation equation (19) is essential in calculating enough coefficients of the continued fraction for an accurate approximation of $I(\Delta\omega)$. In practice, the matrix representation of **A** is generated in the $| f_j \rangle$ basis in which the resulting matrix is complex symmetric

$$\mathbf{A}_{jk} \equiv \langle f_j \mid \mathbf{A} \mid f_k \rangle. \tag{32}$$

From equation (19), the standard recursive relation of the Lanczos algorithm may be rewritten as

$$\beta_{k+1}\,\mathbf{q}_{k+1} = (\mathbf{A} - \alpha_k\mathbf{I})\mathbf{q}_n - \beta_n\,\mathbf{q}_{k-1}, \tag{33}$$

where the column vector $\mathbf{q}_n$ consists of the components $q_{j,k}$ (cf. equation (24)). The standard computer implementation of the complex symmetric Lanczos algorithm [8] can then be used to calculate the coefficients α_j and β_j from which $I(\Delta\omega)$ can be directly calculated using the continued fraction representation given in equation (31).

3.2. THE CONJUGATE GRADIENTS ALGORITHM

The starting point of the conjugate gradients method is to consider the equation

$$| r_k \rangle = | v \rangle - \mathbf{A} \mid u_k \rangle, \tag{34}$$

where $| u_k \rangle$ is the kth approximant to $| u \rangle$, $| r_k \rangle$ is the residual vector associated with $| u_k \rangle$, and **A** is a real symmetric positive definite (RSPD) matrix. The residual vector $| r_k \rangle$ is seen to be the vector which gives the negative gradient of the functional $f[u_k] = \langle u_k \mid \mathbf{A} \mid u_k \rangle - \langle u_k \mid v \rangle$ provided **A** is RSPD [16], so that a minimisation of $f[u_k]$ is equivalent to solving $\mathbf{A} \mid u \rangle = | v \rangle$. Equation (34) is solved by successive iterations which do not minimise along the sequence of vectors $| r_k \rangle$, for $k = 1,2,...,n$, which would be the method of steepest descent, but rather minimise the functional $f[u_k]$ along a set of conjugate directions $| p_k \rangle$ for $k = 1,2,...,n$. This procedure avoids the problem of further minimisation steps spoiling the minimisation along the previous conjugate direction vectors. The conjugate direction vectors $| p_k \rangle$ are defined by

$$| r_{k+1} \rangle = | r_k \rangle - a_k\mathbf{A} \mid p_k \rangle \tag{35}$$

and

$$| p_{k+1} \rangle = | r_{k+1} \rangle + b_k \mid p_k \rangle, \tag{36}$$

where the a_k and b_k are given by

$$a_k = \langle r_k \mid r_k \rangle / \langle p_k \mid \mathbf{A} \mid p_k \rangle \tag{37}$$

$$b_k = \langle r_{k+1} \mid r_{k+1} \rangle / \langle r_k \mid r_k \rangle. \tag{38}$$

The residual vectors are easily shown to be mutually orthogonal but not normalised, while the set

of conjugate direction vectors are **A** conjugate, i.e.,

$$\langle p_j \mid \mathbf{A} \mid p_k \rangle = 0 \qquad \text{if } j \neq k. \tag{39}$$

The vector $\mid p_k \rangle$ is the closest vector to $\mid r_k \rangle$ that is **A** conjugate to the previous conjugate direction vectors. It is also true that $\langle p_j \mid r_k \rangle = 0$ for $j = 1,2,...,k-1$. Also, the $(k+1)$th approximant to the solution vector $\mid u_{k+1} \rangle$ is obtained from $\mid u_k \rangle$ as

$$\mid u_{k+1} \rangle = \mid u_k \rangle + a_k \mid p_k \rangle. \tag{40}$$

These equations permit us to obtain recursively the higher order approximants. That is, let

$$\mid r_1 \rangle = \mid \upsilon \rangle - \mathbf{A} \mid u_1 \rangle \tag{41}$$

and

$$\mid p_1 \rangle = \mid r_1 \rangle, \tag{42}$$

where $\mid u_1 \rangle$ is some initial guess for $\mid u \rangle$. Then, for $k = 1,2,...,n-1$ we calculate, in order, a_k, $\mid u_{k+1} \rangle$, $\mid r_{k+1} \rangle$, b_k and $\mid p_{k+1} \rangle$ using equations (35)-(40). At each step the norm of the residual vector $\mid r_k \rangle$:

$$|| \, r_k \, ||^2 = \langle r_k \mid r_k \rangle \tag{43}$$

is a measure of the deviation of $\mid u_k \rangle$ from the true solution $\mid u \rangle$. Thus the conjugate gradients method permits us to calculate the ESR spectrum, equations (14) and (15), for each point in the spectrum, i.e., for the different values of $\Delta\omega$.

At this stage the Lanczos algorithm and conjugate gradients appear to be very different algorithms, the former tridiagonalises **A** while the latter generates a sequence of approximants to the solution of equation (15). We consider their equivalence later. First we need to consider the applicability of this conjugate gradients method to complex symmetric matrices. It is not hard to show, that for non-defective (i.e., diagonalisable), and non-singular complex symmetric matrices, this conjugative gradients method applies provided only that we use the generalised norm, i.e., rectanormalisation (see equation (29)), just as was found for application of the Lanczos algorithm to complex symmetric matrices. However, for the conjugate gradients method, there is the additional requirement that $\mathbf{A}'(\Delta\omega)$ be non-singular. The complex symmetric matrix **A** will have complex roots: the real parts give the linewidths and the imaginary parts the resonance frequencies. Since all the relevant eigenvalues of **A** must, on physical grounds, have a non-zero real part, then both **A** and **A'** will be non-singular. Nevertheless, it is convenient to replace $i\Delta\omega$ by $i\Delta\omega + T_2'^{-1}$ where $T_2'^{-1}$ is equivalent to an additional linewidth contribution so that we avoid spurious divisions by zero that can occur when $\langle p_k \mid \mathbf{A} \mid p_k \rangle = 0$ in the calculation of a_k (see equation (37)). Zero divisors of this type can be identified as spurious through the construction of the Lanczos tridiagonal matrix from the various quantities generated by the conjugate gradients algorithm as shown in the following section.

3.3. THE EQUIVALENCE OF THE LANCZOS ALGORITHM AND CONJUGATE GRADIENTS METHODS

To make full use of the conjugate gradients algorithm, its equivalence to the Lanczos algorithm must be recognised. First, note that the orthogonal set of vectors $\mid r_k \rangle$ and the conjugate set $\mid p_k \rangle$ are contained in the same Krylov subspace generated by **A** and $\mid \upsilon \rangle$ and the same is true for the Lanczos vectors [12]. Following Golub and Van Loan [12], an explicit expression for the construction of the Lanczos tridiagonal matrix $\mathbf{T}_n$ by the conjugate gradients method for a RSPD

matrix **A** which is valid at each stage of the iteration is,

$$\mathbf{T}_k = \mathbf{D}_k^{-1}\,\mathbf{B}_k^{\dagger}\,\boldsymbol{A}\mathbf{B}_k\,\mathbf{D}_k^{-1}, \tag{44}$$

where $\boldsymbol{A}$ is the diagonal matrix with elements

$$\mathbf{A}_{k,ii} = \langle\, p_i \mid \mathbf{A} \mid p_i \,\rangle, \quad i = 1,2,\ldots,k, \tag{45}$$

and **D** is also diagonal with elements

$$D_{k,ii} = \| r_i \| = \rho_i \equiv \Big(\sum_j y_{i,j}^2\Big)^{1/2}, \quad i = 1,2,\ldots,k, \tag{46}$$

while $\mathbf{B}_k$ is an upper bidiagonal matrix with elements

$$B_{k,ii} = 1, \quad B_{k,i,i+1} = -\,b_i, \quad i = 1,2,\ldots,k;, \tag{47}$$

with b_i given by equation (38). It turns out that the residual vectors are colinear with the Lanczos vectors, more precisely,

$$\mid \Phi_i \,\rangle = \pm\rho_i^{-1} \mid r_i \,\rangle, \quad i = 1,2,\ldots,k. \tag{48}$$

Since the direction of $\mid r_i \,\rangle$ and therefore the signs of its components are well-defined by equation (34), the Lanczos vectors, which are normalised in an arbitrary fashion, bear the sign ambiguity since their direction is not specified by the Lanczos algorithm. It follows from equations (44) to (48) that the matrix elements of $\mathbf{T}_n$ are

$$a_k = \langle\, p_k \mid \mathbf{A} \mid p_k \,\rangle/\rho_k^2 + \big(\rho_k^2/\rho_{k-1}^4\big)/\langle\, p_{k-1} \mid \mathbf{A} \mid p_{k-1} \,\rangle \tag{49}$$

$$b_k = -\,\big(\rho_k/\rho_{k-1}^3\big)/\langle\, p_{k-1} \mid \mathbf{A} \mid p_{k-1} \,\rangle. \tag{50}$$

Thus, the elements α_k and β_k of the Lanczos tridiagonal matrix $\mathbf{T}_n$ are readily obtained from quantities that are calculated by the conjugate gradients algorithm for every step. This approach may be used to generate a tridiagonal matrix approximation to **A** using the conjugate gradients algorithm in the same spirit as the Lanczos algorithm.

In conclusion, the conjugate gradients method can be applied to complex symmetric matrices **A** to give the Lanczos tridiagonal matrix from which spectra may be calculated by the continued fraction technique. The benefit derived from the small amount of extra computational work necessary for the conjugate gradients method as opposed to the Lanczos algorithm method is that an objective criterion for the convergence, r^2 can be monitored at every step. A further benefit is that the conjugate gradients method also allows us to choose selectively those vectors in the basis set that contribute more significantly than others in the calculation of the spectrum [9,17].

4. Relation to Mori's Method in Statistical Mechanics

The application of the Lanczos and conjugate gradients algorithms to the abstract Hilbert space on which the diffusion operator $\tilde{\mathbf{\Gamma}}$ is defined, generates the continued fraction representation of the spectral function. Here we illustrate the close connection of these methods to related methods

involving the calculation of continued fractions from projection operators. A well-known example of the latter is Mori's method [14] used in statistical mechanics for calculating the dynamics of systems of interacting particles. Moro and Freed [13] first showed the formal equivalence between the Mori method and the Lanczos algorithm, and Wassam [18] has described this matter in more detail. It turns out, however, that an even closer correspondence can be achieved between the Mori method and the conjugate gradient method as we now illustrate.

In the Mori method there is a starting vector in Hilbert space which represents the initial value of a relevant dynamical variable. From our previous discussion (see equations (11) to (15)) we can regard $| \upsilon \rangle$ as the starting vector associated with the dynamical variable $P^{\frac{1}{2}} S_j$ and $| u(t) \rangle$ is associated with $\exp(-At) P^{\frac{1}{2}} S_j = \tilde{S}_j(t)$, i.e.,

$$| u(t) \rangle = \exp(-At) | P S_j \rangle = \exp(-At) | \upsilon \rangle. \tag{51}$$

Mori introduces a projection operator $\mathcal{P}_j$ which can be written in our notation as:

$$\mathcal{P}_j = | \Phi_j \rangle \langle \Phi_j | \tag{52}$$

which by comparison with equation (18) shows that

$$P_k = \sum_{j=1}^{k} \mathcal{P}_j, \quad k \leq n. \tag{53}$$

This equation relates the Mori projection operator to the Lanczos projection operator, P_k. Mori then separates $| u(t) \rangle$ into projective and vertical components with respect to the direction $| \upsilon \rangle$. Further projections are continued in Hilbert space to generate a set of orthogonal functions, f_k:

$$\begin{aligned} f_0(t) &\equiv | u(t) \rangle \\ f_j(t) &\equiv \exp(iAt)\, iA f_{j-1}, \quad j \geq 1, \end{aligned} \tag{54}$$

where

$$A_j \equiv (1 - P_k) A = \left(1 - \sum_{j=1}^{k} \mathcal{P}_j\right) A \tag{55}$$

and with complementary functions:

$$f_j \equiv df_j(t)/dt = iL_j f_j. \tag{56}$$

Mori's set of orthogonal functions f_k are closely related to our orthonormal $| \Phi_k \rangle \propto | r_k \rangle$, whereas the complementary functions f_k are related to our $\mathbf{A} | \mathcal{P}_k \rangle$ within simple (normalising) constants. The successive projections (à la Mori) are shown in our present notation in figure 1.

This demonstrates that the Mori projection scheme is formally analogous to the conjugate gradients and Lanczos algorithm ones, and it can be applied to solve the Fokker-Planck equations as well as ESR (and NMR, etc.) lineshape problems. However, a very important point to realise is that whereas these methods are analytically equivalent to one another, these different mathematical realisations give rise to numerical algorithms which differ significantly in their numerical reliability and stability. Careful numerical analyses have demonstrated that the Lanczos algorithm and the conjugate gradients method are the methods of choice in terms of the stability and efficiency of the numerical algorithms required to implement them on a computer.

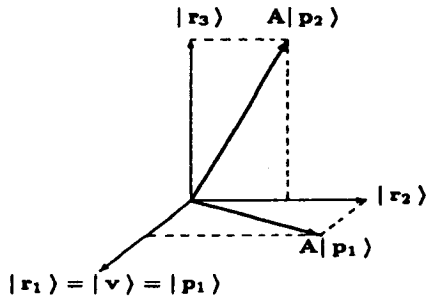

Figure 1. Schematic relation between vectors: $|\mathbf{r}_1>$, $\mathbf{A}|\mathbf{p}_1>$, $|\mathbf{r}_2>$, $\mathbf{A}|\mathbf{p}_2>$ and $|\mathbf{r}_3>$. $|\mathbf{r}_3>$ and $|\mathbf{r}_2>$ denote the vertical component of $\mathbf{A}|\mathbf{p}_2>$ and the orthogonal component of $\mathbf{A}|\mathbf{p}_1>$, respectively.

5. Ordering and Thermodynamics: Behaviour of Large versus Small Probes

5.1. TEMPERATURE STUDIES

The extent of probe ordering in a liquid-crystalline environment depends on the size and geometrical anisotropy of the probe, and the preferred location of the probe amongst the solvent molecules. In general, we expect larger (and more axially symmetric) probes to be more ordered than smaller (and more spherically symmetric) ones. Such behaviour is best illustrated with reference to an example: the orientational ordering of the four probes perdeuteriated tempone-d_{16}, MOTA, P and CSL in the mesomorphic phases of 4O.6, 4O.8, Phase V, S2, and 6OCB-8OCB (the sizes of the probes increase in the order shown). The temperature variation of the order parameters

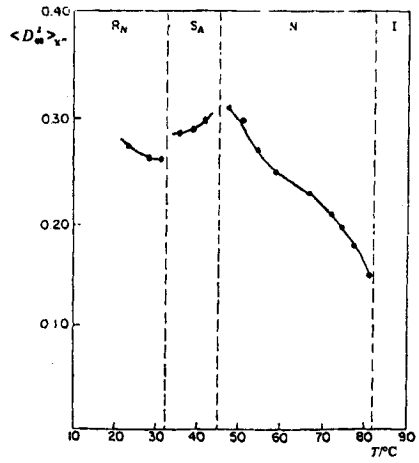

Figure 2. The temperature variation of the order parameter $<D^2_{00}>$ for P in the phases of 6OCB-8OCB. (From [21]).

of these probes in these liquid crystal solvents is shown in table 6 in Chapter 12, and table 1 shows how different probes sample different regions in the smectic phases of liquid crystals [19]. In general, an increase in ordering with probe size is observed, with however, the exception of MOTA in 6OCB-8OCB, which is actually less ordered than perdeuteriated tempone-d_{16} in spite of being larger than the latter [21]. This was not observed to be the case in 4O.6 (i.e., perdeuteriated tempone-d_{16} is less ordered than MOTA in 4O.6). The apparent discrepancy can be reconciled on the basis of the hypothesis that while in 4O.6 MOTA prefers to pack with the cores, it prefers packing among the chains in 6OCB-8OCB, whereas in both solvents perdeuteriated tempone-d_{16} packs with the cores in the nematic phase (however, with the likelihood that probe expulsion to the chain regions occurs in 6OCB-8OCB as the S_A phase is approached).

Table 1. Slow motional ESR spectra in smectic phases.
How different spin probes sample different regions in smectic phases.

Liquid Crystal	4O.8/4O.6	S2	8CB	5CB Low Temp.	Phase V High Temp.	Phase V Low Temp.	DPPC L_α
PD-Tempone	I	I	I		I	Phase separation	I
CSL	I	I	I		I	I	I,II
Doxyl Fatty acids (or doxyl-labeled lipids	I	I	I		I	I	I,II
POATP (propionyl deriv. of Tempamine)	I	I	I		I	II	I
P	I	II	II	II	I	II	Interlayer Location
Stearamide	I	II	II		I	II	Interlayer Location

Reproduced with permission from Meirovitch E. and Freed, J.H. (1984) J. phys. Chem., **88**, 5003.
I ≡ region I ≡ uniaxial smectic A type alignment of local directors usually associated with the rigid core region.
II ≡ region II ≡ distribution of local directors usually associated with the flexible alkyl chain region.

It will also be noted that the ESR spectra of CSL in the S_A phase of S2 is sensitive to higher order spherical harmonics ($L = 4$) [19] in the expansion of the ordering potential (see Chapter 4) than those typically used for the others ($L = 2$). Reasonable fits to the spectra, however, could be obtained using $L = 2$ for CSL in the smectic phases of 4O.6 and 4O.8, [26] which are known to form monolayer smectics (S2 forms a bilayered S_A phase), but the $L = 4$ terms were not utilised in those studies. We show later how the use of non-linear least squares fitting of the simulations to experiment can provide an objective criterion for estimating which, and how many, expansion parameters in the ordering potential can realistically be estimated from the experiments. In both 4O.6 (and 4O.8) and S2, the high ordering suggests that CSL reorients in an environment which is mainly composed of the rigid core regions. It does not therefore experience any cooperative effects of chain distortions which would lead to a distribution of local directors such as that

believed to be experienced by the P probe in S2 (see later) [25].

5.2. PRESSURE-TEMPERATURE STUDIES

Hwang et al. [20] have shown that the ordering of the spin probe as a function of temperature and pressure carries some relevance for theories of the nematic state. Their results on such measurements show that the probe order parameter $S^{(p)}$ is a monitor of the thermodynamic properties of the solvent. Assuming a Maier-Saupe potential, and letting $u_2^{pp}/k_BT = a^{pp}/V^{\gamma_p}T$ and $u_2^{ss}/k_BT = a^{ss}/V^{\gamma_s}T$, where u_2 is the coefficient of the potential of mean torque in the mean field approximation and superscripts p and s stand for probe and solvent respectively. It can be shown that [20]

$$\left(\frac{\partial \ln S^{(s)}}{\partial \ln T}\right)_V = \frac{(\Delta S^s)^2 a^{ss}/V^{\gamma_s}T}{1 + (\Delta S^i)^2 a^{ss}/V^{\gamma_s}T}. \tag{57}$$

In this equation, $(\Delta S^{(s)})^2$ is the mean square fluctuation in the order parameter given by

$$(\Delta S^{(s)})^2 \equiv < \left(D_{00}^{2(s)}\right)^2 > - < D_{00}^{2(s)} >^2 \tag{58}$$

and γ is defined by:

$$\gamma \equiv - (\partial \ln T/\partial \ln V)_S \tag{59}$$

with a similar equation for probe ordering [20]. McColl et al. [22] found γ_s to be 4 for another liquid crystal PAA, but our result $\gamma_p = 2.9 \pm 0.1$ in the perdeuteriated tempone-d_{16}/Phase V system [23] suggests that $\gamma_p \leq \gamma_s$. A more general treatment of this problem is given by Cotter [24]. In her simulations, the length-to-breadth ratio of a liquid crystal is the crucial parameter that essentially determines the γ. The actual value of γ_s for Phase V is not known. The correlation of the γ_p with γ_s would be important in the studies of solvent-solute interactions. Clearly, pressure and temperature dependent ESR studies of liquid crystal like probes would be extremely valuable in clarifying these matters further.

6. Dynamics in I, N, S_A and N_R phases

In this section, we shall consider ESR studies of rotational dynamics in liquid crystals performed using spin probes that typically exhibit incipient slow motional (i.e., P-probe) or slow motional spectra (e.g., CSL), as opposed to the studies described in Chapter 12 with perdeuteriated tempone-d_{16} where most of the results could be treated in terms of motional narrowing theory. A distinct advantage of studies in the slow motional regime is that it is often possible to distinguish between different models of spin relaxation owing to the greater sensitivities of the relaxation parameters to dynamics when the correlation frequencies τ_R^{-1} are of the order of the anisotropy in the spin hamiltonian. Using the P-probe and CSL (see Chapter 12, figure 3) as spin probes, we shall describe relaxation studies in the isotropic and ordered phases of some liquid crystals, and compare them with similar studies using perdeuteriated tempone-d_{16} (cf. Chapter 12). In particular, studies of P and CSL in 4O.6, 6OCB-8OCB and S2 will be described; the first of these liquid crystals forms a mono-layer S_A phase, while the latter two form bilayered S_A phases (with 6OCB-8OCB exhibiting a re-entrant nematic phase (N_R)).

6.1. ISOTROPIC PHASE

As noted in table 2, the mean rotational correlation time (defined as $\tau_R = (1/6)(D_R^{\parallel} D_R^{\perp})^{-1/2}$, where $D_R^{\parallel}$ and $D_R^{\perp}$ denote the components of the rotational diffusion tensor) for P lie between 76-200 ps in 4O.6, 110-1100 ps in S2, and 200-900 ps in 6OCB-8OCB. This trend is consistent with the results for perdeuteriated tempone-d_{16} in these liquid crystals (see Chapter 12), where the motional rates in the cyanobiphenyls were also noted to be somewhat longer than in 4O.6. However, we note that τ_R for P probe is about an order of magnitude higher than for perdeuteriated tempone-d_{16}, as can be expected for a larger probe.

Table 2a. Order parameters and mean correlation times for P in 4O.6.

T/°C	Mesophase	λ_{20}	λ_{22}	$\langle D_{00}^2 \rangle$	$\langle D_{02}^2 + D_{0-2}^2 \rangle$	$\tau_R / 10^{-11}$ s	*N*	E_{act}/kJ mol^{-1}
100.1	Isotropic	0.0	0.0	0.0	0.0	7.7	7.0	38.1
72.5		0.0	0.0	0.0	0.0	20.0		
71.7	Nematic	1.17	0.0	0.26	0.0	17.4	14.0	29.2
50.5		2.00	0.0	0.44	0.0	34.0		
49.5	Smectic A	2.15	0.0	0.47	0.0	37.0	10	(20.5)
49.5		2.50	-0.6	0.53	-0.14	40.0	20	(20.9)
43.3		2.20	0.0	0.48	0.0	43.0	10	(20.5)
43.3		2.90	-0.7	0.60	-0.16	46.0	20	(20.9)
42.5	Smectic B	3.10	0.0	0.62	0.0	120.0	3	39.7
42.5		4.8	-1.7	0.76	-0.37	125.0	3	41.4
23.3		3.8	0.0	0.70	0.0	225.0	3	39.7
23.3		5.0	-1.8	0.77	-0.38	231.0	3	41.4

Reproduced with permission from Meirovitch E. et al. (1982) J. chem. Phys., **77**, 3915.

Table 2b. Order parameters and mean correlation times for P in S2.

T/°C	Mesophase	λ_{20}	λ_{22}	$\langle D_{00}^2 \rangle$	$\langle D_{02}^2 + D_{0-2}^2 \rangle$	$\tau_R / 10^{-11}$ s	*N*	E_{act}/kJ mol^{-1}
100.1	Isotropic	0.0	0.0	0.0	0.0	11.0	6	50.2
47.0		0.0	0.0	0.0	0.0	111	6	50.2
46.0	Nematic	.97	0.0	0.21	0.0	135	(6)	-
44.5	Smectic A	1.0	-0.5	0.22	-0.12	170	4	6.2
-9.0		6.0	-0.8	0.82	-0.18	320	4	6.2

Reproduced with permission from Meirovitch E. et al. (1982) J. chem. Phys., **77**, 3915.

Table 2c. Order parameters and mean correlation times for P in 6OCB-8OCB.

T/°C	Mesophase	λ_{20}	λ_{22}	$<D^2_{00}>$	$<D^2_{02}+D^2_{0-2}>$	$\tau_R/10^{-11}$ s	N	E_{act}/kJ mol^{-1}
104.2	Isotropic	0.0	0.0	0.0	0.0	13.0	4	54.0
99.8		0.0	0.0	0.0	0.0	16.0	4	54.0
90.8		0.0	0.0	0.0	0.0	25.0	4	54.0
84.8		0.0	0.0	0.0	0.0	33.0	4	54.0
80.9	Nematic	0.76	0.0	0.15	0.0	35.0	10	31.4
77.0		0.93	0.0	0.18	0.0	38.0	10	31.4
74.1		1.10	0.0	0.22	0.0	41.0	10	31.4
71.2		1.16	0.0	0.23	0.0	45.0	10	31.4
66.5		1.22	0.0	0.24	0.0	50.0	10	31.4
58.7		1.36	0.0	0.27	0.0	66.0	10	31.4
54.3		1.46	0.0	0.29	0.0	80.0	10	31.4
51.1		1.56	0.0	0.31	0.0	90.0	10	31.4
47.3		1.62	0.0	0.32	0.0	98.0	10	31.4
40.5	Smectic A	1.51	0.0	0.30	0.0	190	15	10.5
38.6		1.46	0.0	0.29	0.0	295	15	10.5
36.2		1.46	0.0	0.29	0.0	200	15	10.5
30.3	Reentrant	1.22	0.0	0.24	0.0	350	11	28.0
27.7		1.22	0.0	0.24	0.0	377	11	28.0
23.0		1.36	0.0	0.27	0.0	460	11	28.0

Reproduced with permission from Nayeem A. and Freed J. H. (1989) J. phys. Chem., **93**, 6539.

Fits to the spectra using P-probe typically required the use of an anisotropic diffusion model, with a value of $N(N \equiv D_R^{\parallel}/D_R^{\perp})$ lying between 4 (6OCB-8OCB) and 7 (4O.6). Using a prolate ellipsoid model for P with the long axis dimension of 10 Å and the short axis dimension of 2.85 Å, an N of 4 is estimated [25]. The higher values of N that have been observed imply that it is likely that along with the overall $D_R^{\parallel}$ some internal motion of the piperidine ring is also occurring. The detailed temperature dependence of τ_R, shown in figures 3a-c, shows an activation energy of 38.1 kJ mol^{-1} in 4O.6, 50 kJ mol^{-1} in S2, and 54.0 kJ mol^{-1} in 6OCB-8OCB. At this point, it is interesting to compare the temperature dependences of τ_R [or $\tau_R^{\perp} \equiv 1/(6D_R^{\perp})$] for P in 4O.6, S2 and 6OCB-8OCB with perdeuteriated tempone-d_{16} in the same (or similar) solvents (see figures 5b, d and e in Chapter 12). Such comparisons show the activation energies for the two probes to be quite similar: For perdeuteriated tempone-d_{16}, we have ΔE_{act} = 33.9 kJ mol^{-1} in 4O.6, ΔE_{act} = 62.3 kJ mol^{-1} in 8CB, and ΔE_{act} = 52.7 kJ mol^{-1} in 6OCB-8OCB. The interesting point here is that

in spite of the motion of P being much slower than perdeuteriated tempone-d_{16} (consistent with the larger size of the former), there is a close similarity of the ΔE_{act} within the isotropic phase. In fact, we even note such similarities in the nematic phase.

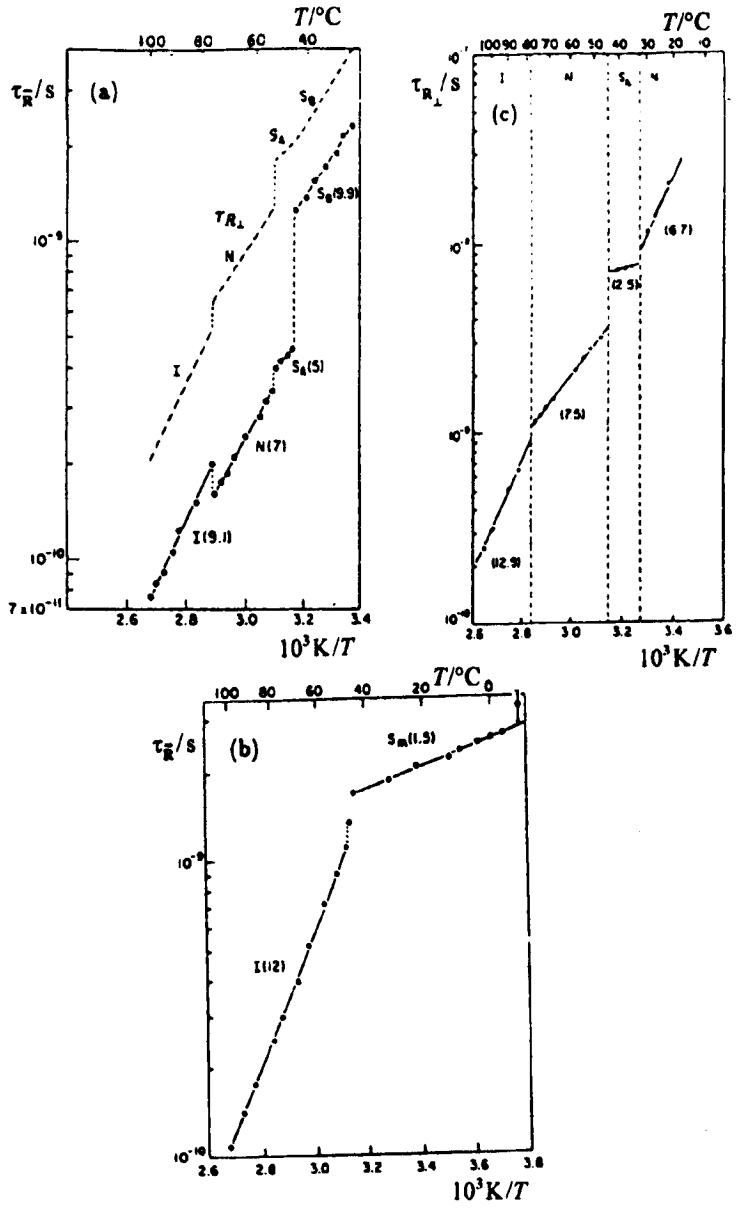

Figure 3. τ_R versus $1/T$ for P in (a) 4O.6; (b) S2 and (c) 6OCB-8OCB. (From [21] and [25]).

Whereas the width of the nematic phase in S2 (about 1.5°C) precludes a reliable analysis of dynamics within this phase, detailed analyses of the relaxation rates of P in the nematic phases of 4O.6 and 6OCB-8OCB show that in both solvents N increases by a factor of two from its value in the I phase (see table 2), while $\tau_R^{\perp}$ only increases by 10-20%. This indicates that $D_R^{\parallel}$ increases at a significantly faster rate than $D_R^{\perp}$. Moreover, ΔE_{act} decreases in the N phase compared to the I phase in both solvents (see table 2).

As compared with perdeuteriated tempone-d_{16} in the isotropic phases of 4O.6 and 6OCB-8OCB, we again note that the activation energies in the nematic phases of these solvents with the two probes are rather similar, and in both cases (i.e., perdeuteriated tempone-d_{16} and P) they decrease in the nematic phase compared to their values in the I phase. These general observations suggest that in spite of their differences in size and geometry, perdeuteriated tempone-d_{16} and P behave rather similarly in their dynamic properties in the I and N phases. The decreased ΔE_{act} in the N phase suggests that both probes seem to be experiencing greater dynamic interactions with the chain regions.

Studies using the larger spin probe CSL have also been performed in 4O.6 (and 4O.8) [26] and S2 [19]. In these cases, the results of the slow motional lineshape analysis, shown in table 3, indicate $N \approx 5$ in 4O.6 and 4O.8 (N is estimated to be about 4.7 for CSL, see [27] where Rao et al. used $N = 4.7$ to simulate successfully their spectra for CSL in the nematic phase of Phase V). The rotational correlation times are higher (i.e., slower motion) than P; e.g., in 4O.6 $\tau_R \approx$ 2-3.8ns for CSL [26] compared with $\tau_R \approx$ 174-340 ps for P in 4O.6 [25], while the activation energies are comparable in the two cases (29-31 kJ mol^{-1}). In fact, it has also been noted that ΔE_{act} is comparable for perdeuteriated tempone-d_{16} and CSL in Phase V, showing that, as with perdeuteriated tempone-d_{16} and P, the dominant dynamic mode of reorientation of CSL in the nematic phase of these solvents can be treated as a simple diffusive reorientation of a partially ordered probe in a uniaxial medium.

Table 3a. Rotational diffusion coefficients and order parameters for CSL in 4O.8.

T/°C	Mesophase	λ_{20}	$\langle D_{00}^2 \rangle$	$D_R^{\parallel} / 10^8\ s^{-1}$	$D_R^{\perp} / 10^7\ s^{-1}$	N	E_{act}/kJ mol^{-1}
76.8	Nematic	2.7	0.40	2.08	3.6	5.8	≈ 25.1
73.0		4.1	0.57	1.85	3.3	5.6	
67.7		6.2	0.73	1.67	2.9	5.8	
62.4		6.5	0.74	1.39	2.5	5.6	
59.5	Smectic A	6.5	0.74	1.4 ± 0.15	0.93 ± 0.15	15	
53.0		9.0	0.82	1.2 ± 0.20	0.20 ± 0.15	60	
46.9		11.0	0.86	1.0 ± 0.30	0.04 ± 0.03	250	
45.5	Smectic B	11.5	0.87	≈ 1.0 ± 0.30	> 0.01	≈ 1000	
30-15		> 13	> 0.89	≈ 1.0 ± 0.30	> 0.01	≈ 1000	

Table 3b. Rotational diffusion coefficients and order parameters for CSL in 4O.6.

T/°C	Mesophase	λ_{20}	$\langle D^2_{00}\rangle$	$D^{\parallel}_R / 10^8\,s^{-1}$	$D^{\perp}_R / 10^7\,s^{-1}$	N	E_{act}/kJ mol^{-1}
71.0	Nematic	2.3	0.35	2.10 ± 0.15	4.2 ± 0.5	5	≈ 31.4
56.6		5.5	0.68	1.20 ± 0.15	2.4 ± 0.3	5	
51.0		7.3	0.77	1.00 ± 0.2	2.0 ± 0.3	5	
49.4	Smectic A	7.3	0.77	1.00 ± 0.2	0.56 ± 0.1	18	
44.0		11.0	0.86	0.85 ± 0.30	0.02 ±0.01	450	
42.2	Smectic B	11.0	0.86	0.85 ± 0.30	0.02 ± 0.01	450	
20.0		13.0	0.88	≈ 0.85 ± 0.30	> 0.01	850	

Reproduced with permission from Meirovitch E. and Freed J. H. (1980) J. phys. Chem., **84**, 2459.

Table 3c. Rotational diffusion coefficients and order parameters for CSL in the smectic A phase of S2.

T/°C	λ_{20}	λ_{22}	λ_{40}	λ_{42}	$\langle D^2_{00}\rangle$	$\langle D^2_{0-2}+D^2_{02}\rangle$	$\langle D^4_{00}\rangle$	$\langle D^4_{02}+D^4_{0-2}\rangle$	$D^{\parallel}_R/10^6\,s^{-1}$	$D^{\perp}_R/10^6\,s^{-1}$	N	E_{act}/kJ mol^{-1}
40.0	1.7	0.0	0.0	0.0	0.38	0.0	0.0	0.0	149.0	32.0	≈5	50.2
25.0	1.25	0.23	0.73	0.1	0.34	0.06	0.17	0.03	70.4	15.0		
09.0	3.10	0.40	1.0	0.2	0.73	0.03	0.44	0.05	24.2	5.0		
1.0	3.20	0.60	1.15	0.32	0.75	0.05	0.47	0.07	11.6	2.5		
-8.0	3.0	1.0	1.00	0.55	0.69	0.1	0.40	0.14	4.8	1.0		

Reproduced with permission from Meirovitch E. and Freed J. H. (1984) J. phys. Chem., **88**, 4995.
Note that $\lambda_{20} = 3\lambda_{20}/2$ in tables 3a and 3b.

6.3. SMECTIC A PHASE

It is in the S_A phase that P and CSL show their differences in dynamic behaviour from perdeuteriated tempone-d_{16}. While the activation energies for perdeuteriated tempone-d_{16}, P and CSL were noted to be rather similar in the N phase (and in the I phase for the P-probe), a significant decrease in ΔE_{act} is noted for P in 4O.6, S2 and 6OCB-8OCB. (Note that with perdeuteriated tempone-d_{16} (see figure 3, Chapter 12, ΔE_{act} decreased from 35.1 (N) to 17.6 (S_A) kJ mol^{-1} in 4O.6, but increased from 17.2 (N) to 35.6 (S_A) kJ mol^{-1} in 8CB, and from 25.9 (N) to 36.0 (S_A) kJ mol^{-1} in 6OCB-8OCB.) Furthermore, given the larger size of P compared to perdeuteriated tempone-d_{16}, the activation energies in the bilayer S_A phases (S2 and 6OCB-8OCB) were abnormally low (6.3 kJ mol^{-1} in S2 and 10.5 kJ mol^{-1} in 6OCB-8OCB).

In analogy to perdeuteriated tempone-d_{16}, the interpretation of the relaxation results for P is as follows. The significant decrease in ΔE_{act} for perdeuteriated tempone-d_{16} in the S_A phase was

interpreted in terms of this small probe being expelled in the lower temperature phase from the rigid core region of the smectic layer (due to increased packing) towards the more fluid alkyl chain region [28,21] (see also Chapter 12, section 4.3.2.). It was speculated that P may be experiencing greater dynamic interactions with the alkyl chain regions of the liquid crystal in passing from I-N-S_A. This would be consistent with a gradual reduction in its activation energy. However, the increasing order parameter with decreasing temperature suggests that unlike perdeuteriated tempone-d_{16}, P may not be completely expelled from the rigid core regions, even though interaction with the alkyl chains may be playing an increased role in its dynamics.

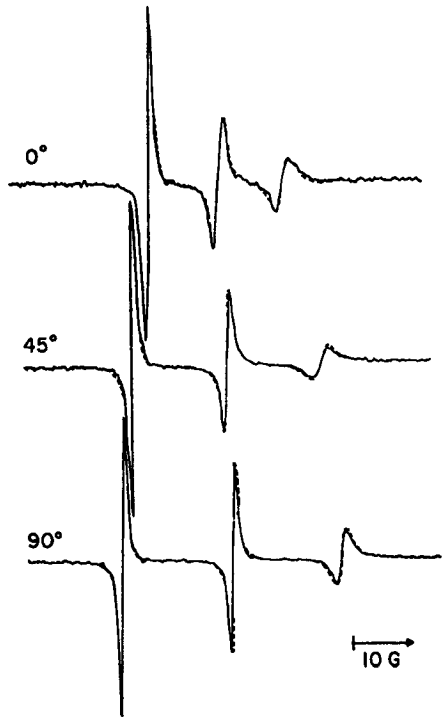

Figure 4. Angular dependent spectra of P in the S_A phase at 49.5°C of S2 with simulations (—) using $\lambda = 2.5$, $\rho = -0.6$, $D_R^{\perp} = 10^8\ s^{-1}$, $N = 20$ and $T_2^{*-1} = 0.4$ G. (From [25]).

As noted in Chapter 12, section 4.3.2., the director in the S_A phase can be locked in, thereby allowing us to perform angle dependent relaxation studies as described for perdeuteriated tempone-d_{16} in S2 [29]. In figure 4, we show angle dependent spectra for P in S2 as a function of director orientation (relative to the field) together with the simulations. A distinct advantage of such studies is that upon simulating the lineshapes as a function of the director orientation, we can place more reliability on the dynamic parameters than those obtained from a single simulation at one orientation. An interesting and unusual feature is observed in the spectra of P in S2 as the temperature in the S_A phase is lowered and the ordering increases. The ESR spectra become spread over a wide magnetic field range, and additional peaks appear. These features are not observed in the smectic S_A and S_B phases in the monolayer smectic forming 4O.6, and may be an important

difference between monolayer and bilayer S_A phases from a molecular dynamic viewpoint. That is, while in monolayer smectics, spectra are observed that are typical of nitroxide probes dissolved in a well-aligned and uniaxial medium with a single well-defined director, the spectra (at lower temperatures) in the S_A phase of S2, a bilayer smectic, suggests some kind of distribution of directors. Proceeding on the assumption that the dynamics of P is influenced mainly by the chain motions, we have found that a model involving the cooperative distortion mode of the chains is successful in explaining the unusual features. Figure 5 shows a comparison of the experimental spectra of S2 in the S_A phase with simulations based on this model. (Such features were not noted for P in the S_A phase of 6OCB-8OCB [21], possibly because the ordering was not high enough for these effects to be observed. The N_R phase appeared before the ordering was sufficiently high.)

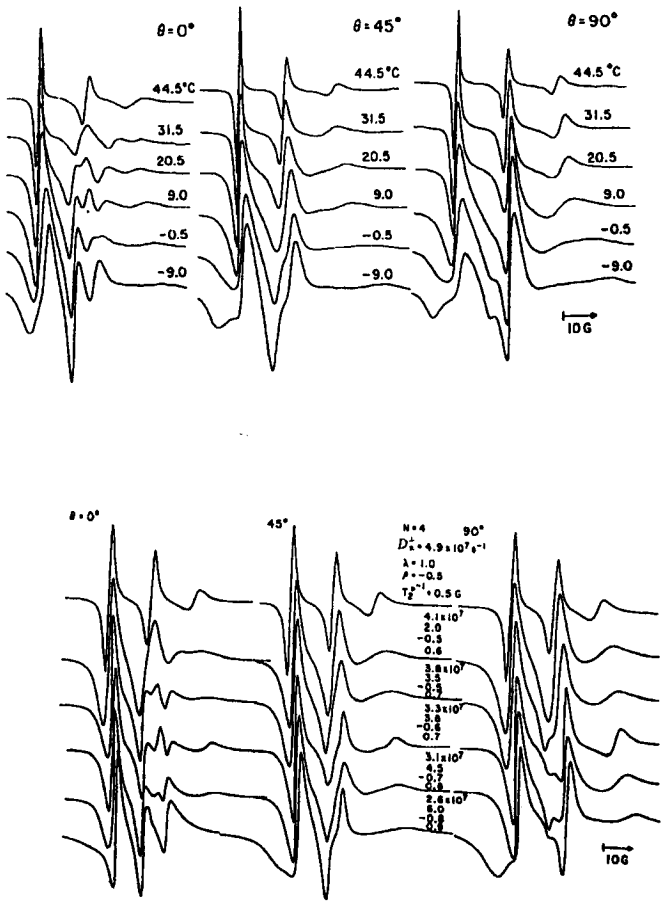

Figure 5. (a) Experimental spectra of P in the S_A phase of S2 showing the additional peaks at lower temperatures; (b) Simulations using the cooperative distortion model. (From [25]).

Studies performed using CSL, which exhibits significantly higher ordering (and slower motion) than P, have shown that either (i) the values of N required to fit the spectra in the S_A phases are abnormally large (for example, for 4O.6 N lies between 18-450, and for 4O.8, N = 15-250) [26], or (ii) when N is kept constant at 4.7 (the value used for CSL in Phase V [27], many coefficients in the ordering potential expansion (see section IB) are needed to simulate the results. Thus, Meirovitch and Freed [19] have employed four terms in the ordering potential to fit oriented spectra of CSL in S2, as we have already discussed. The apparent value of N in the former case is clearly untenable with a brownian type of diffusive model, and is interpreted as indicative of significant deviations from brownian behaviour. An approximate model involving fluctuating torques was suggested in interpreting the anomaly. The observations were explained in terms of the effect of the local solvent structure on the nature of the overall dynamic structure of the probe, implying considerable local cooperativity in these smectic phases [26]. Case (ii), while showing that a brownian model is probably appropriate for describing the diffusion of CSL in S2, demonstrates the considerable sensitivity of these spectra to the symmetry of the orienting potential. However, in both cases, the likelihood of the involvement of a fluctuating torque mechanism seems appropriate.

6.4. SMECTIC C PHASE

ESR studies of spin relaxation in the S_C phase of HOAB using the CSL spin probe have also been performed [26]. Because of the symmetry of the S_C phase, unless special care is exercised in sample alignment, macroscopically disordered samples can result from cooling the system into the S_C phase. Monodomain S_C samples were prepared by (i) sandwiching the HOAB between glass plates to obtain sufficiently thin samples so that the S_C director would not realign upon rotating the field away from parallel alignment with the director, and (ii) cooling the mesogen from the (higher) N phase in a strong magnetic field (ca. 21 kG) oriented at about 45° relative to the normal to the glass plates. When prepared in this way, the ESR spectra were essentially S_A-like, but with a director tilted (at 45°) with respect to the normal to the smectic layers [26]. In contrast to CSL in other liquid crystal solvents we have studied (i.e, 4O.6, 4O.8, Phase V), CSL exhibits fast motion in HOAB [26]. Linewidth measurements (see Chapter 12) show $D_R^{\perp}$ to lie in the range $0.16 - 0.35 \times 10^9\ s^{-1}$, with N varying between 11 and 20, with high ordering ($< P_2 > = 0.83 - 0.88$).

6.5. REENTRANT NEMATIC PHASE

Our recent ESR studies on 6OCB-8OCB (cf. Chapter 12, section 4.3.2.) [21] were performed with the motivation of discerning possible differences between this reentrant mixture and liquid crystals which, in spite of being structurally similar to 6OCB-8OCB and also exhibiting (like the latter) bilayer S_A phases, do not exhibit a reentrant nematic phases (cf. P in S2 versus P in 6OCB-8OCB). These studies have shown that:

(i) In both cases (reentrant and non-reentrant liquid crystals) the probes behave very similarly in their dynamic properties; they are expelled towards the alkyl chains as smectic layers begin to form. Perdeuteriated tempone-d_{16} and MOTA, though mainly in the chain regions, can however partially experience the aromatic cores, while the P-probe is completely buried in the chains.

(ii) The orientational ordering of the aromatic cores increases gradually through the N, S_A and N_R phases in a fashion that is not sensitive to these phase transitions. This is monitored by the CSL probe, which shows typically high ordering ($< P_2 > \sim 0.7 - 0.8$). Such results are basically the same for reentrant and non-reentrant liquid crystals (see figure 6; cf. also [30]).

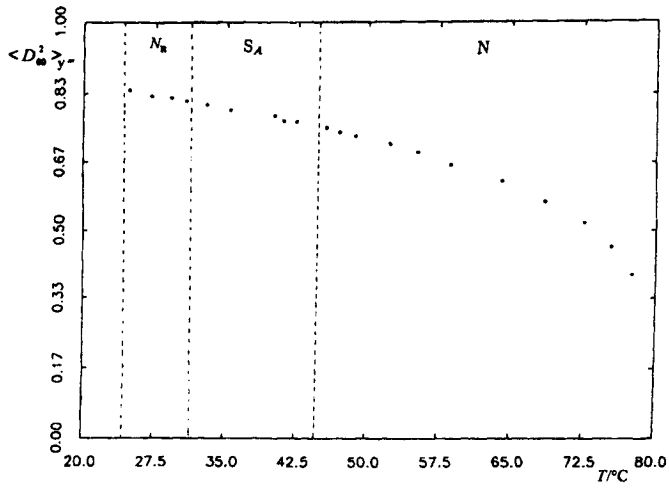

Figure 6. The temperature variation of the order parameter for CSL in 6OCB-8OCB. (From [21]).

(iii) Results on the ordering and dynamics of P-probe in the reentrant nematic liquid crystal suggest that the chains are more disordered in the S_A and N_R phases compared to the N_R phase of a normal smectic, whereas they experience enhanced resistance to rotational motion in the N_R phase, probably due to enhanced packing in the chain region. This is suggestive of reduced short range chain cooperativity in ordering and dynamics as increased packing of chains from adjacent layers occurs concomittent with the loss of smectic order.

(iv) In general, the nematic and S_A phases in systems exhibiting reentrance are rather similar to those in structurally similar liquid crystals where reentrance is not observed. At the molecular level, the S_A-N and N_R-S_A transitions are similar, and the effects driving the transition are subtle. Small changes in molecular properties can make a difference, i.e. the decrease in average chain length by the addition of 6OCB to 8OCB to produce a reentrant nematic. Previous X-ray [31] and density [32] results also demonstrate the similarities of these phase transitions with nothing dramatic occurring.

7. Rotational Dynamics in Lyotropics: Lipid Multilayers

We now discuss some applications of ESR to the study of selected problems in membrane biophysics. The subtle dynamical aspects of membrane structure can play significant roles in biological functions. For example, the cooperative motions in phospholipids can influence the degree of permeability of cell membranes, and the ordering and dynamics at different points along the lipid chains provide a quantitative measure of the chain flexibility. The extent to which such flexibilities are affected by the presence of intrinsic membrane protein provides some information on the nature of lipid-protein interactions.

Interestingly, the L_α phase of lipids is very similar to the smectic A phase found in thermotropic liquid crystals. We have conducted systematic ESR studies of oriented bilayers as a function of the concentration of the polypeptide gramicidin and of cholesterol. Our studies employ both the

conventional CW ESR as well as newly developed time domain ESR techniques.

7.1. DYNAMIC MOLECULAR STRUCTURE AND PHASE TRANSITIONS IN LIPID MULTILAYERS

The use of defect-free oriented samples enabled us to observe clearly lipid phase transitions through the appearance of composite spectra at the transition (two phase) region [33]. From ESR observations on low water content DPPC and DMPC (cf. figure 7) three phase transitions were found over a temperature range below 180°C: two were assigned to the main transition and to the isotropic transition by reference to the transition temperatures in the literature. The remaining one, at 100-110°C, was characterised as a new chain orientational transition.

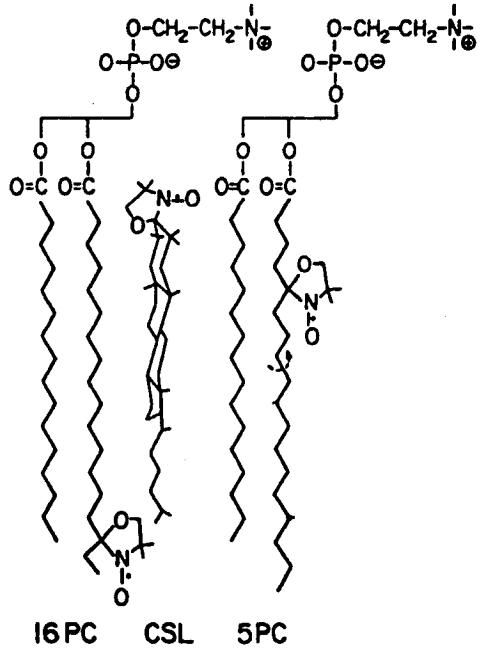

Figure 7. Schematic structures of CSL, 5PC and 16PC. (From [33]).

The ordering and the rotational diffusion tensor of the various spin labels could be determined accurately as a function of temperature, % H_2O, and phase (see table 4). CSL, 5PC and 16PC (cf. figure 7) exhibit in all phases decreasing order parameters S, according to CSL > 5PC > 16PC and increasing motional rate (measured by D_R the mean rotational diffusion coefficient) again according to CSL < 5PC < 16PC, while the anisotropy in rotational motion obeys CSL > 5PC > 16PC, consistent with the well-known concept of the increased flexibility on moving down the chain [34]. However, we have been able to quantify this flexibility gradient in terms of its reduced ordering and its symmetry, as well as the increased motional rate [33].

Using these results we can characterise the main [or gel-to-L_α] transition as primarily a chain diffusional transition, while the new high temperature transition is characterised as a chain orientational transition: the order parameter S experiences a more significant relative reduction at the second transition compared to that at the main transition, whereas the diffusion coefficient $D_R^{\perp}$

Table 4. Parameters for molecular ordering and anisotropic rotation of CSL in DPPC[a,e].

T/°C	Phase[b]	$< D_{00}^2 >$[d]	$< D_{02}^2 + D_{0-2}^2 >$[d]	$D_R^{\perp}$[c]/s^{-1}	$D_R^{\parallel}$/s^{-1}	N	E_{act}/kJ mol^{-1}	T_2^{*-1}/G
				(A) Hydrated to 3 wt %				
40	I	0.90	-0.01	2.9×10^5	4.4×10^7			
50		0.90	-0.01	4.0×10^5	6.0×10^7	150	32.2	1.5
60		0.90	-0.01	6.2×10^5	9.3×10^7			
70		0.90	-0.01	8.3×10^5	1.2×10^8			
80	II	0.76	-0.03	6.8×10^6	3.4×10^8			
85		0.73	-0.03	8.0×10^6	4.0×10^8	50	36.4	1.2
90		0.67	-0.03	9.6×10^6	4.8×10^8			
110	III	0.28	0.08	1.1×10^8	1.7×10^9			
120		0.21	0.06	1.5×10^8	2.4×10^9			
130		0.14	0.03	2.0×10^8	3.2×10^9	16	38.5	1.0
140		0.13	0.03	2.5×10^8	4.0×10^9			
160	IV	0	0	5.8×10^8	2.9×10^9			
170		0	0	6.7×10^8	3.4×10^9			
180		0	0	7.5×10^8	3.8×10^9	5	20.9	1.0
				(B) Hydrated to 7 wt %				
40	I	0.88	-0.005	3.0×10^5	4.5×10^7			
50		0.88	-0.005	5.0×10^5	7.5×10^7	150	36.4	1.5
60		0.88	-0.005	7.0×10^5	10.5×10^7			
70	II	0.78	-0.007	9.0×10^6	4.5×10^8			
80		0.74	-0.009	1.2×10^7	6.0×10^8	50	29.3	1.2
90		0.65	-0.015	1.6×10^7	8.0×10^8			

[a] Estimated errors: ±2% in $< D_{00}^2 >$, ±30% in $< D_{02}^2 + D_{0-2}^2 >$, ±10% in $D_R^{\perp}$, ±20% in N, ±20% in E_{act}, and ±0.1 G in T_2^{*-1}. Note that $D_R^{\parallel} = ND_R^{\perp}$.

[b] I: biaxial gel phase; II and III; liquid-crystalline phases; IV: isotropic phase.

[c] Correlation times: $\tau_{\perp} = (6D_R^{\perp})^{-1}$, $\tau_{\parallel} = (6D_R^{\parallel})^{-1}$, and $\tau_R = (6D_R^{\perp}D_R^{\parallel})^{-1/2}$.

[d] The relationship between $< D_{00}^2 >$, $< D_{02}^2 + D_{0-2}^2 >$ and λ and ρ is given by the expression: $< D_{00}^2 > = \int d\phi' \int d\theta' P(\theta',\phi')(1/2)(3\cos^2\theta' - 1)\sin\theta'$ and $< D_{02}^2 + D_{0-2}^2 > = \int d\phi' \int d\theta' P(\theta',\phi')$ $(\sqrt{6}/2)\sin^2\theta' \cos 2\phi' \sin\theta'$, where θ' denotes the angle between the principal z' axis of the ordering tensor and the principal z'' axis of the director frame. $P(\theta',\phi')\sin\theta' d\theta' d\phi'$ is the distribution of z' relative to z'' given by $P(\theta',\phi') \propto \exp[(-1/2)(3\cos^2\theta' - 1) + \sqrt{6}\rho \sin^2\theta' \cos 2\phi']$.

[e] Reproduced with permission from Tanaka H. and Freed J. H. (1984) J. phys. Chem., **88**, 6633.

for the chain probes (i.e., 5PC and 16PC) experiences a more significant relative increase at the main transition. Thus, a relatively smaller reduction in molecular ordering more effectively unfreezes the chain motions at the main transition compared to the second one. The relative increase in $D_R^{\perp}$ for CSL at the two transitions is, however, comparable suggesting that while local chain motion increases more significantly at the main transition, the overall molecular motions exhibit comparable relative changes at both transitions. Also, whereas $D_R^{\perp}$ shows substantial change at the phase transitions, $D_R^{\parallel} = ND_R^{\perp}$, which measures the motion about the long chain axis, is much less affected. This undoubtedly reflects the existence of significant motion of this type in the gel phase, which may be due to its relatively unhindered nature. Finally, we find that at both phase transitions there is a more significant relative reduction in ordering at the end of the chain but a smaller increase in fluidity (as measured by $D_R^{\perp}$). Thus, while there is a greater melting of orientational order at the end of the chain, the end chain motions are not as significantly tied to the ordering.

7.2. EFFECT OF CHOLESTEROL ON LIPID DYNAMICS

The effect of cholesterol on the diffusion of lipid molecules has attracted much attention because it is directly related to understanding the dynamic properties of biological membranes. A conspicuous feature of the phase diagram of cholesterol-lipid systems is that at concentrations of cholesterol exceeding 20 to 30 mole per cent, a phase boundary is observed which has characteristics similar to the main chain melting transition (T_m); i.e., a kind of gel to liquid-crystalline phase boundary, implying that it is a considerably disordered fluid state above 20 (to 30) mole per cent of cholesterol. In addition to such phase behaviour, the dynamical properties and ordering of the molecules in the bilayer have their own importance, and these have been studied both by fluorescence techniques [35] (see also Chapter 22) as well as by magnetic resonance methods [36] (see also Chapter 21).

Studies using fully hydrated bilayers have shown that (i) in the liquid-crystalline state, the major effect of cholesterol is to reduce the angular range for rotational motion without decreasing the mobility substantially [35], while (ii) in the gel phase, cholesterol induces local disorder and enhances the rotational motion. More specifically, the addition of cholesterol has the following effects: (i) below T_m, the fluidity increases, i.e., the ordering decreases and the motional rates increase; (ii) above T_m, the fluidity decreases, i.e., ordering increases, while the motional rates decrease. These observations are consistent with the detailed ESR observations of Shin and Freed [36]. On the other hand, careful studies of CSL in low water content DPPC multilayers by ESR showed effects of cholesterol on the rotational dynamics similar to that in the liquid-crystalline phase even in the gel phase [37]. Both below and above T_m, the fluidity was noted to decrease. However, the fluidity was noted to increase at what appeared to be a third phase at higher temperatures (above the L_α phase).

7.3. LIPID-GRAMICIDIN INTERACTIONS

Given that the interpretation of ESR spectra from dispersions is somewhat ambiguous, we have adapted our alignment methods of sample preparation to prepare very well-aligned uniform samples containing the stable polypeptide gramicidin A. This polypeptide is frequently used to mimic the effects of protein on phospholipid bilayers [38]. Its advantages are its known chemical structure and its known helical conformations, its considerable stability, and its ready availability. Chapman and co-workers [38] have found that the dimeric gramicidin A is incorporated into the

lipid bilayer, and they regard it as a model for the interactions of the polypeptide segments of transmembrane proteins within the hydrocarbon regions of the lipid bilayers.

The principal findings are as follows [39]. (i) In the gel phase we have observed distinct two component spectra which could be assigned to highly oriented bulk lipids and to a disordered component, and the latter was fit by a model of molecular disorder such that the ordering of these molecules is greatly reduced, but their rotational-motional properties are not appreciably changed (cf. figures 8a and 9a). The disordered region at the lowest concentration of gramicidin A is estimated to consist of about 30-40 lipid pairs, or about five times the number required to coat the gramicidin A dimer. This corresponds to a disordered region in the bilayer extending over about three lipid molecules. This effect of disordering is significantly reduced by increasing the weight per cent of water, but it appears to be independent of temperature. (ii) In the liquid-crystalline phase, heterogeneity is not distinguished from the ESR spectrum. Instead, the primary effect of gramicidin A is to reduce significantly the observed ordering of all the lipids, with only a very small decrease in motional rates [cf. figures. 8b and 9b]. However, in the high temperature, weakly ordered phase, addition of gramicidin A actually leads to a significant increase in ordering. This increase in ordering is also observed in high water content dispersions in the immobilised species in any of the spectra obtained from well-aligned samples. However, such features are present in dispersion samples of 4M% gramicidin A prepared from the same materials as the well-aligned ones. If we associate these spectral features with trapped lipids due to aggregation of gramicidin A, then it follows that macroscopically well-aligned samples do not allow for such aggregation.

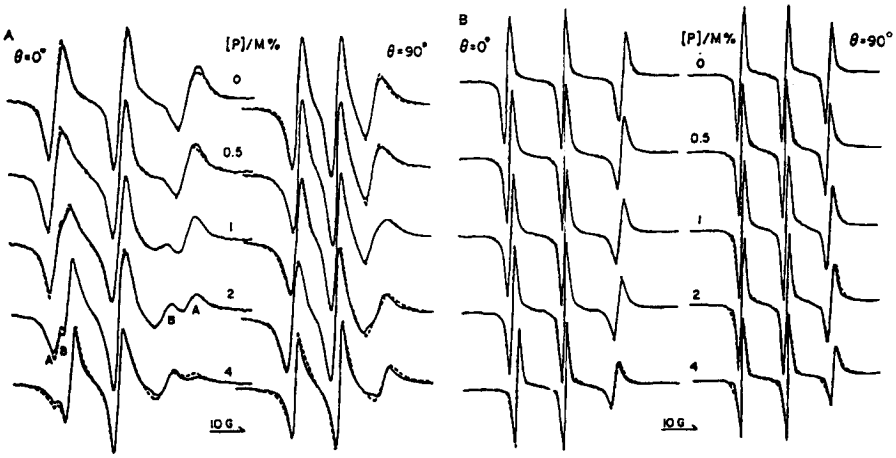

Figure 8. ESR spectra from 16PC in DPPC hydrated to 7wt% for GA concentrations ranging from 0 to 4 mole per cent. Spectra are shown for $\theta=0°$ and $\theta=90°$: (a) 50°C corresponds to the gel phase; (b) 80° corresponds to the lamellar phase. Dashed spectra are simulations. In (a), the ordered and disordered components are labelled A and B, respectively. (From [39]).

We conclude from these findings that the principal lipid-gramicidin A interaction is that of a boundary effect such that the gramicidin A induces disorder in the low temperature and low water content lipids, but it induces order for high temperature and high water content (i.e., less ordered) lipids. It has only slight effects on lipid fluidity, in general reducing only slightly the rates of

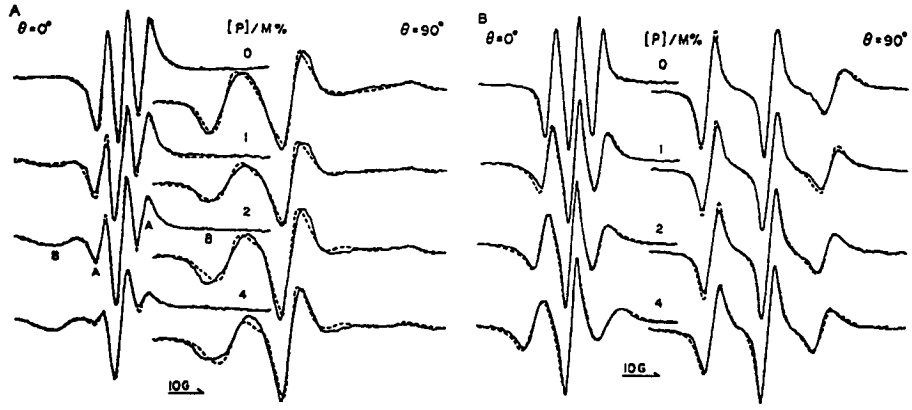

Figure 9. ESR spectra from CSL in DPPC hydrated to 7wt% for GA concentrations ranging from 0 to 4 mole per cent. Spectra are shown for $\theta=0°$ and $\theta=90°$: (a) 50°C corresponds to the gel phase; (b) 80° corresponds to the lamellar phase. Dashed spectra are simulations. In (a), the ordered and disordered components are labelled A and B, respectively. (From [33]).

rotational reorientation.

We believe that these various effects can be explained as the consequence of two competing features of the lipid-gramicidin A interaction: a disordering feature and a hardening feature. The former induces a disordering of the lipids in their vicinity, while the latter makes them more solid-like, as exemplified by the somewhat reduced fluidity and by increasing the order. Furthermore, we require that disordering is dominant under conditions of low fluidity, while hardening is dominant when there is high fluidity. The notion of two apparently opposite effects of the macromolecules on the ordering of lipids has been incorporated into a simple model by Jahnig [40]. He proposed that the ordering at the boundary of a protein should be lower than that for the ordered phase but greater than that for the fluid phase. Our low water content results are consistent with this model when we apply it to the phase transition between the L_α to high temperature liquid crystal phase.

The heterogeneity induced by gramicidin A at very low concentrations is a distinctly different phenomenon from that usually assigned to immobilised or trapped lipids. The clear discrimination of the heterogeneity in the bilayer induced by the gramicidin A, and the determination of the molecular properties of this heterogeneity should be significant in understanding the polypeptide-lipid interaction.

8. Experimental Techniques: Lineshapes in One and Two Dimensions

Millhauser and Freed [41] have shown that in the slow motional regime, when the CW ESR spectra become very inhomogeneously broadened, significantly better resolution to motional dynamics can be achieved by producing two dimensional electron spin echo spectra. We shall now compare the two dimensional techniques with the one dimensional one, and illustrate the greater sensitivity of the former in obtaining more detailed dynamic information through studies of the

homogeneous linewidth, T_2. The two examples considered later are: (i) the effect of motional anisotropy on the one dimensional versus two dimensional spectra, and (ii) the orientation dependence of such spectra from multilayers of low water content DPPC doped with CSL spin probe.

The electron spin echo experiment, which essentially measures the decay rate of a Hahn echo as a function of the resonant field, involves sweeping through the static magnetic field B_0 very slowly, but with a microwave field intensity B_1 small enough that only dynamic spin packets associated with widths well within the inhomogeneous width Δ are effectively rotated by the pulses (see also Chapter 8 for the NMR analogue). Technical details of the experiment are provided elsewhere [29].

The form of the two dimensional ESE spectrum is given by:

$$S(\omega,\omega') \propto \sum_j a_{jj} \frac{T_{2j}}{1 + \omega^2 T_{2j}^2} \exp\left[-(\omega' - \omega_j)^2/\Delta^2\right] \qquad (60)$$

which is a sum of lorentzians along the ω axis (the Fourier transform of τ) and the sum of gaussians along the ω' axis (the Fourier transform of t). By this means, the relaxation of each spin packet (i.e., T_{2j}) is displayed. Furthermore, while the resonance position of the spin packet (i.e., ω_j) is given along the ω' axis, the variation of T_{2j} across the spectrum is given along the ω' axis. In other words, we can thus achieve a resolution of the different dynamic behaviour of the various spin packets.

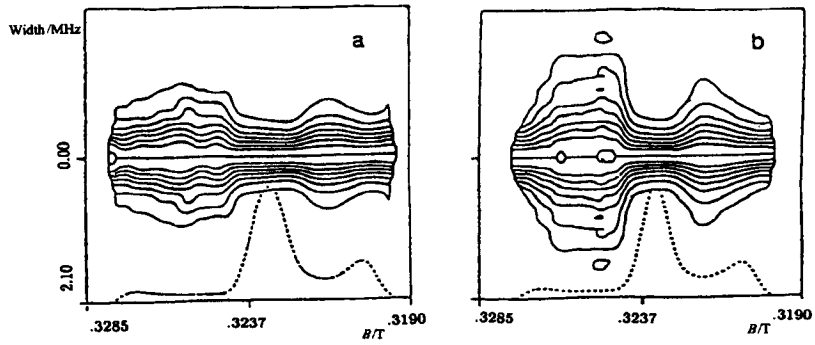

Figure 10. Normalised contours and 0 MHz slices from spectra of: (a) Tempone in 85% glycerol/water at -75°C; (b) CSL in n-butylbenzene at -135°C. [From G. L. Millhauser, Ph.D. thesis, Cornell University (1986)].

The data are most usefully displayed by normalised contours. These are produced by dividing $S(\omega,\omega')$ by the zero MHz slice (i.e., $S(0,\omega')$) to normalise and then to display the constant contour lines (and also the zero MHz slice). A set of horizontal lines imply that there is no T_2 variation across the spectrum, whereas contour lines with curvature indicate the presence of at least some variation. We find that these contours are very sensitive not only to the rate of reorientation but also to the model of molecular reorientation, (i.e., whether it is by jumps, free diffusion, or brownian motion) with different characteristic patterns for each. We show in figure 10 an experimental demonstration of the sensitivity to motional anisotropy by comparing the results for tempone, which tumbles nearly isotropically with that for CSL, whose motion is anisotropic.

While the T_2's are comparable, the contour shapes are significantly different, emphasising the large anisotropy for CSL. It should also be emphasised that figure 10 shows patterns that are consistent with a brownian reorientation model. In the general theoretical analysis of this experiment, Millhauser and Freed [41] show that brownian reorientation, which occurs by infinitesimal steps, will lead to a T_2 variation, because of the different sensitivity of different spectral regions to a small change in molecular orientation (i.e., $dS(\omega')/d\theta$ varies across the spectrum). On the other hand,reorientation by substantial jumps would not show any T_2 variation.

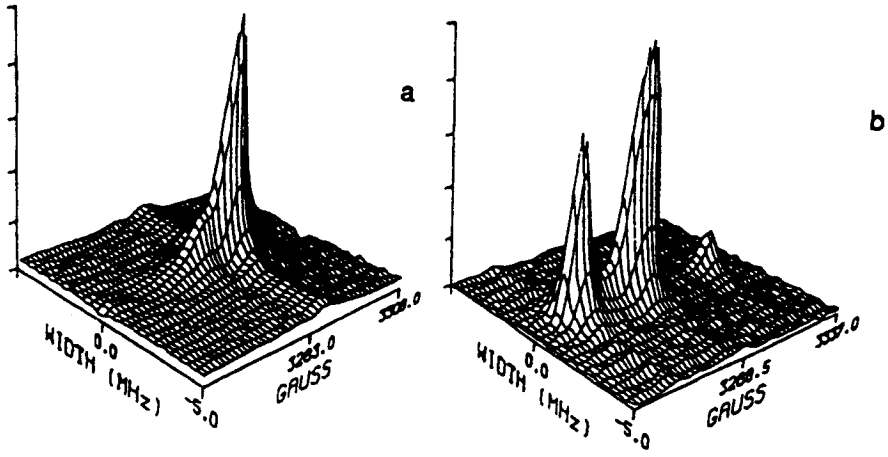

Figure 11. Experimental 2D-ESE spectra from CSL in oriented multilayers of low water content DPPC: (a) θ=0°, T=-20°C; (b) θ=90°, T=-20°C, where θ denotes the director orientation relative to the field. The "width" axis provides the homogeneous lineshape, whereas the "Gauss" axis supplies the ESR inhomogeneous lineshape. (From [42]).

The two dimensional ESE technique has also been applied to oriented phospholipid samples [42] (cf. figure 11). In figure 12, we show a sequence of experimental contours and zero MHz slices from oriented multilayers of low water content dipalmitoyl phosphatidyl choline (DPPC) doped with cholestane spin label (CSL) for different temperatures and orientation θ, and in figure 13 we show typical simulations which relate to these results (in particular, figure 12a) showing specific sensitivities to the orienting potential as well as details of the dynamics. We wish to emphasise the importance of this sensitivity. Our studies with CSL in oriented lipid samples have shown that even in the slow motional region, where CW spectral simulations are only slightly sensitive to motion, it is very difficult to obtain a unique set of parameters characterising the system [33,39]. In fact, temperature dependent inhomogeneous broadening may dominate the CW EPR lineshapes in the very slow motional region. In the CW lineshape analysis, there is a danger of misinterpreting this effect as due to motion. The two dimensional ESE results are much more sensitive to these matters as illustrated in the simulations shown in figure 14. In figure 14a we show a CW EPR simulation for high ordering ($<P_2>$ = 0.87) and very slow motion $D_R \approx 10^4\ s^{-1}$. We superimpose the results for isotropic (N = 1) and very anisotropic (N = 100) motions to demonstrate that they are almost indistinguishable. However, in figures 14b and 14c we show the two dimensional ESE contours and 0MHz slices for the same parameters. They clearly differ both in magnitude and shape and are very easily distinguishable.

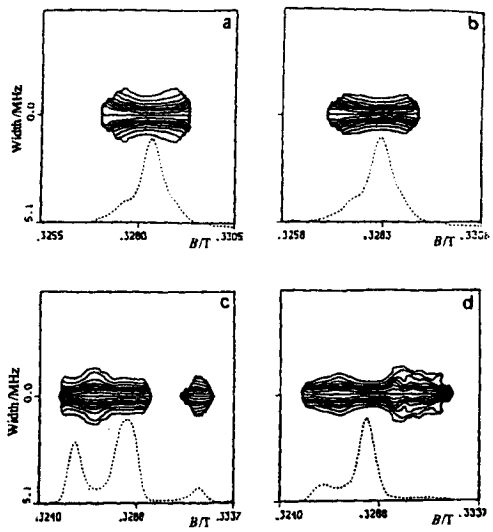

Figure 12. Normalised contours of spectra from CSL in low water content DPPC multilayers: (a) θ=0°, T=0°C; (b) θ=0°, T=-20°C; (c) θ=90°, T=-20°C; (d) θ=45°, T=-20°C. (From [42]).

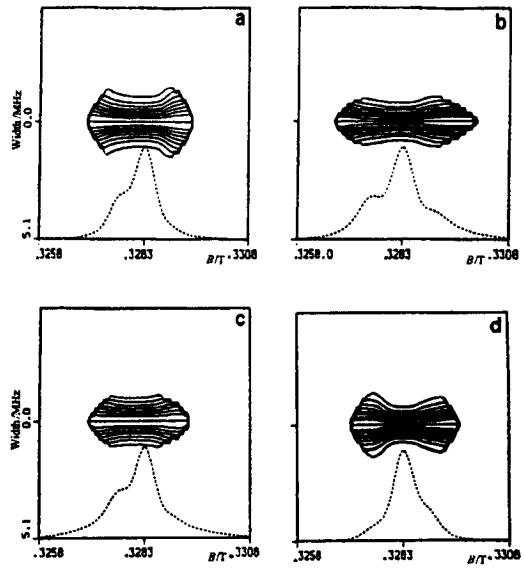

Figure 13. Normalised contours and 0MHz slices of simulated DPPC/CSL oriented spectra (θ=0°) to illustrate the sensitivity to motion and ordering. (a) $D_R^I = 4 \times 10^4\ s^{-1}$, N=5, S=0.85; (b) $D_R^I = 2 \times 10^4\ s^{-1}$, N=4, S=0.85; (c) $D_R^I = 1 \times 10^4\ s^{-1}$, N=1, S=0.70; (d) $D_R^I = 1 \times 10^4\ s^{-1}$, N=1, S=0.90. The effects of an intrinsic (solid state) T_2 (0.7 μs) and inhomogeneous broadening (0.32 mT) have been included. (From [42]).

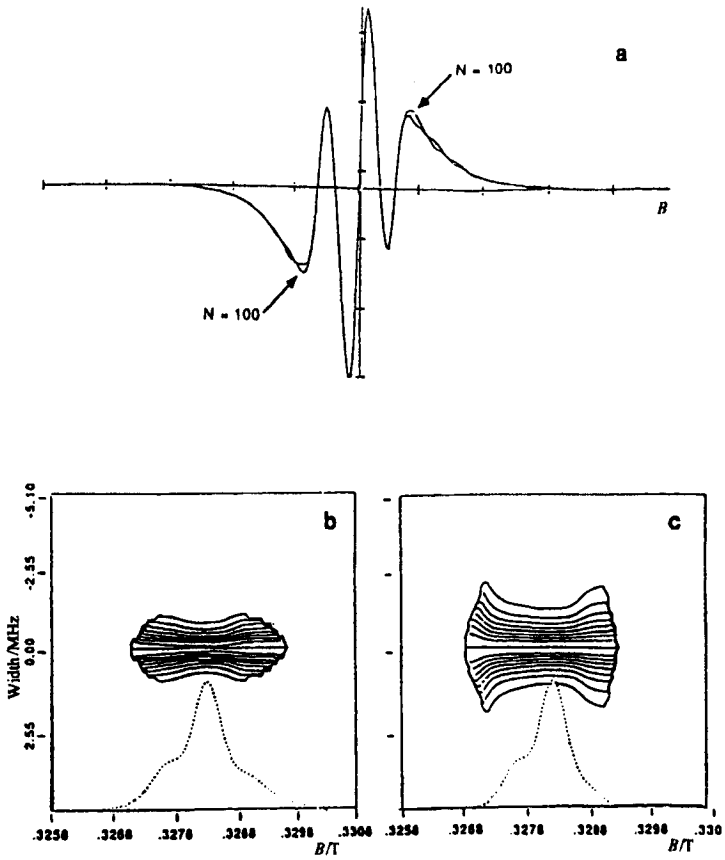

Figure 14. Comparison of the relative sensitivity of CW against 2D-ESE to motional anisotropy. (a) Two superimposed simulations, where one spectrum has $D_R^{\perp} = 10^{-4}$ s^{-1} and $N=1$, and the other has the same $D_R^{\perp}$ but with $N=100$. The markers on the x axis are 9.77 G apart. The normalised contours are simulated from the same parameters with (b) $N=100$, and (c) $N=1$. Here, $S=0.87$ and $\theta=0°$ (director orientation) was used. (From [45]).

It is this sensitivity to dynamics and ordering that may be exploited in many biophysical applications. For example, we have obtained well-aligned two dimensional ESE spectra for higher water content samples (20 wt.%H_2O) prepared by a combined evaporation and annealing method. Several plate samples are stacked together to increase signal strength. Typical results are shown in figure 15. These are interesting because they show significant variation of T_2 across the spectrum, more than previously obtained for lower water content (cf. figure 13), and this should enhance the ability to distinguish structure and dynamics. [n.b. New two dimensional ESR techniques based upon Fourier transform methods have recently been developed [47,48] which significantly enhance the sensitivity to motional dynamics in the slow motional regime.]

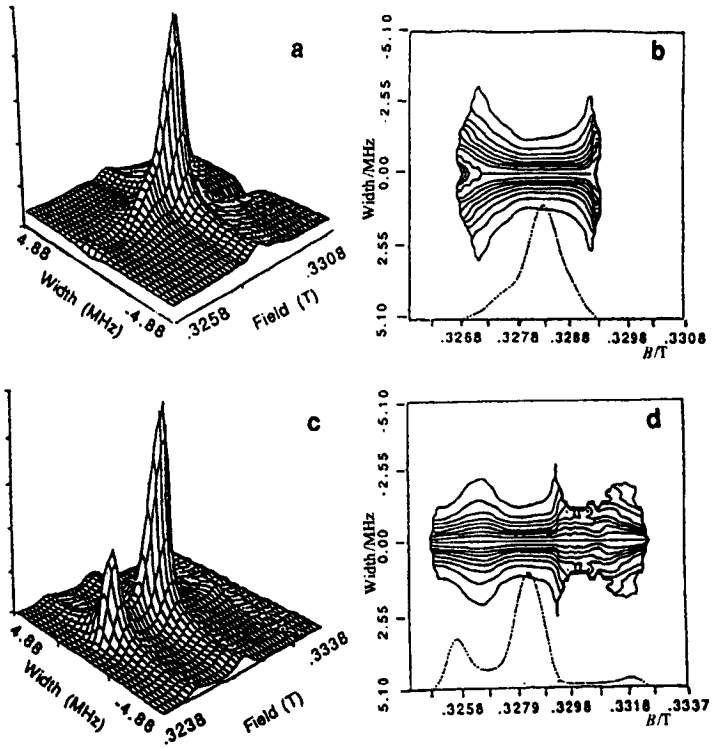

Figure 15. 2D-ESE spectra of CSL in high water content (20 per cent by wt.) DPPC at -40°C. (a) and (b) show the spectrum and associated contours for θ=0°; (c) and (d) are for θ=90°.

9. On Fitting the Data

9.1. NON-LINEAR LEAST SQUARES

In the slow motional ESR regime, simulations of the experimental spectra often require the simultaneous variation of several parameters (i.e., $D_R^{\parallel}$, $D_R^{\perp}$, coefficients in the ordering potential and contributions due to inhomogeneous broadening T_2^{*-1}) in order to obtain reasonable fits to the spectra. The number of such parameters can increase dramatically as more sophisticated dynamical models are used. As the number of parameters to be varied increases, we are confronted with the problem that several choices of parameters can lead to fits of similar quality, and then a more quantitative criterion becomes necessary to discern the fits.

We have developed a non-linear least squares procedure based on the Levenberg-Marquardt algorithm [43] that can vary the user specified parameters within selected ranges, and calculate successive ESR spectra until the fits based on the choice of parameters converge within the radius specified by the user. This procedure has the two-fold advantage that (i) it saves a considerable

amount of user time in that the programme (rather than the user) varies the parameters in accordance with well-established methods (i.e., steepest descent) to reach the best-fit, and (ii) it provides a quantitative measure of goodness of fit, i.e., in terms of the sum of squared differences between experimental and fitted spectra.

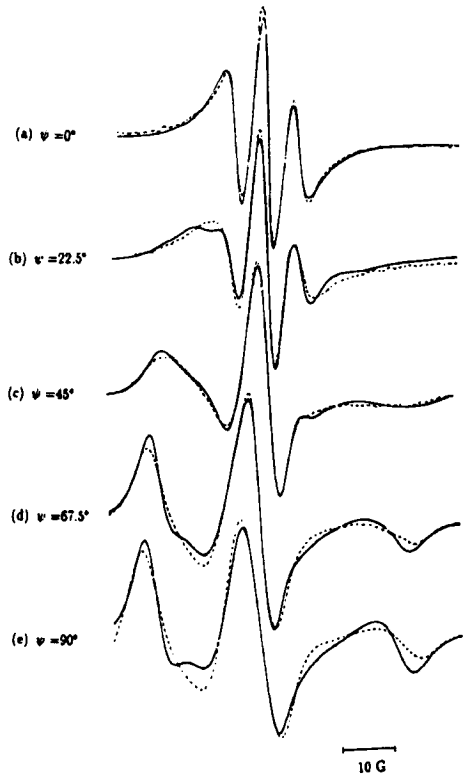

Figure 16. Simulated spectra of CSL in the S_A phase at -8°C using a non-linear least squares procedure. The parameters used were: $D_R^{\perp} = 1.84 \times 10^6\ s^{-1}$, $D_R^{\parallel} = 19.17 \times 10^6\ s^{-1}$, $\lambda_{20} = 2.21$, $\lambda_{22} + \lambda_{2-2} = -0.47$, $\lambda_{40} = 1.10$, $\lambda_{42} + \lambda_{4-2} = -0.57$; while a molecular tilt (i.e., orientation of the diffusion frame relative to the magnetic tensor frame) of (0°, 12°, 90°) was used (but kept fixed). Director orientation relative to the field was (a) 0°, (b) 22.5°, (c) 45°, (d) 67.5°, and (e) 90°. (From [44]).

An example of the application of our procedure to the simulation of the orientation dependent spectra of CSL in the S_A phase of S2 is shown in figure 16 [44], and in figure 17 we show the originally fitted spectra for comparison [19]. The reasons for this particular choice (i.e., CSL in the S_A phase of S2) are that (i) it has often proved to be difficult to fit all orientation dependent spectra using the same set of ordering and dynamic parameters, and (ii) the simulations here require the use of four terms in the ordering potential, and $N = 4.7$ (see table 3). The use of our non-linear least squares fitting procedure helps in deciding if the fits may have been better with a high value of N and using one order parameter (i.e., as was noted for CSL in other liquid crystals [27,26]). The best fits using this procedure are shown to be consistent with an increased value of N (about 10), but they also require a four term ordering potential. The improved quality

of our fits as compared to the previous simulations (with the possible exception of the 90° spectrum) justify the use of non-linear least squares fitting for slow motional spectra. The extension of this method to spectra from more complicated systems, such as CSL in DPPC [37] is presently under way.

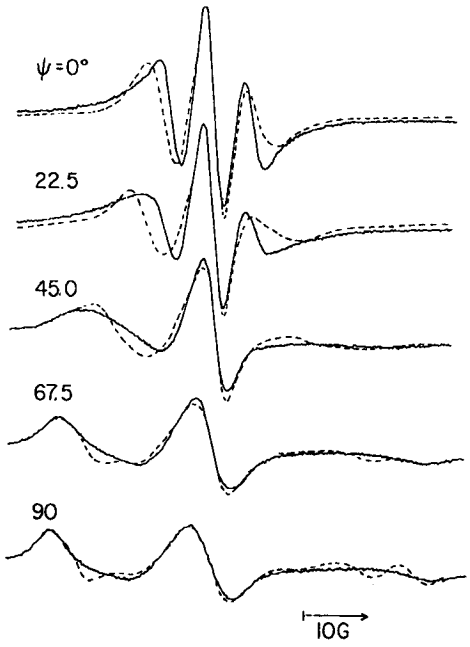

Figure 17. Same as in figure 16 but without using a non-linear least squares. The parameters were $D_R^{\perp} = 2.0 \times 10^6\ s^{-1}$, N=4.7, $\lambda_{20} = 3.0$, $\lambda_{22} + \lambda_{2-2} = -1.0$, $\lambda_{40} = 1.10$, $\lambda_{42} + \lambda_{4-2} = -0.55$; while a molecular tilt (i.e., orientation of the diffusion frame relative to the magnetic tensor frame) of (0°, 15°, 90°) was used (but kept fixed). Director orientation to the field: (a) 0°, (b) 22.5°, (c) 45°, (d) 67.5°, and (e) 90°. (From [19]).

9.2. THE LPSVD METHOD

An important experimental artifact of the two dimensional ESE technique is the effect of a non-zero dead time τ_d after the second pulse, that partly arises due to cavity ringing. Consequently, equation (60) includes a factor $\exp[-2\tau_d/T_{2j}]$ for the finite deadtime, i.e., we are limited to times $\tau > \tau_d$. A technique of data analysis applied by Millhauser and Freed [45], viz. linear prediction with singular value decomposition, enables us to back extrapolate the two dimensional ESE data set to estimate the signal in the range $0 < \tau < \tau_d$. This method also leads both to significantly improved resolution enhancement of the complex two dimensional lineshapes as well as to the least-squares values characterising the exponential decays associated with the echoes [45]. Furthermore, it removes a difficulty with fast Fourier transform methods; that is, to avoid so-called fast Fourier transform window effects, it is necessary to collect data over a considerable time range before performing the transform. This means that a considerable amount of time is spent collecting data when the signal-to-noise ratio is low, and, hence, the spectral resolution is low.

Instead, with linear decomposition, we need only collect over those time ranges for which there is a significant signal, thereby greatly increasing the efficiency of the data acquisition; these features are illustrated in figure 18.

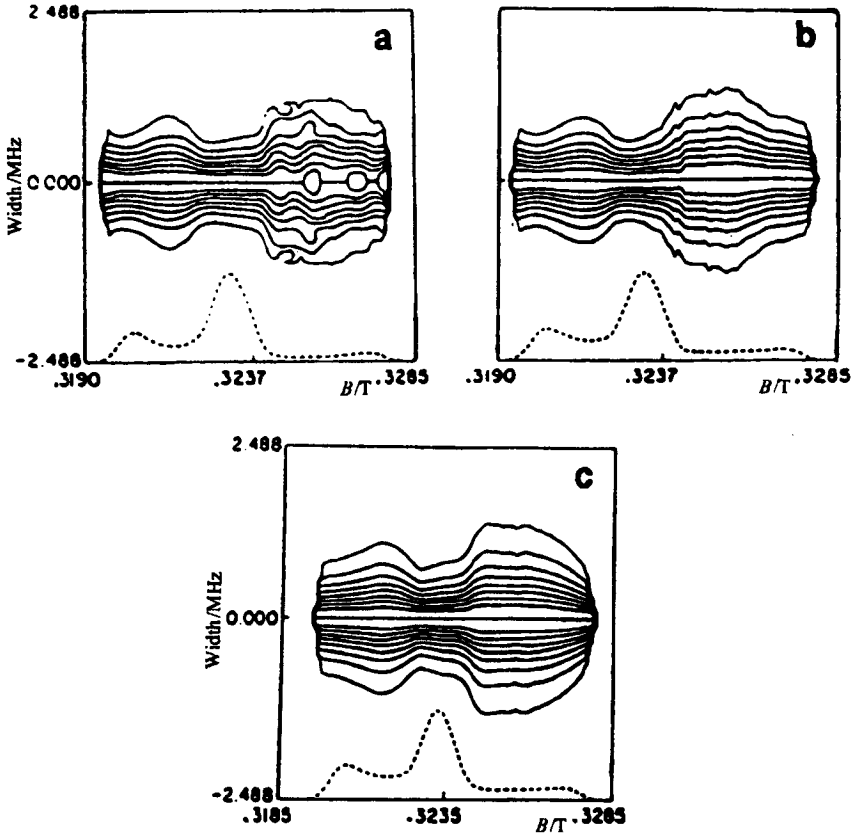

Figure 18. Normalised contours showing resolution enhancement obtained from the LPSVD treatment. (a) Perdeuteriated tempone in 85% glycerol-water at -75°C treated by conventional FFT; (b) from the same data set, but treated with LPSVD; (c) different data set collected from the same system in a manner that maximises the efficiency of the LPSVD algorithm. (From [45]).

Thus, we have found that the use of linear decomposition in the data analysis leads to a much more powerful and useful two dimensional ESE method. It means much better discrimination of detail in the two dimensional contours which translates into a much better analysis of molecular dynamic structure. Its ability to recover signal from noise means, that as long as we are able to obtain echoes yielding an estimate to T_M by usual procedures, then useful two dimensional ESE contours may be obtained with the use of linear prediction decomposition. This is an important development for liquid crystal and model membrane studies. For low water content samples [37] it was possible to obtain estimates of T_M from ESE over most of the temperature range from +140°C to -150°C for both CSL and the phospholipid spin label 16-PC. However, only a restricted

range (cf. figure 6) could yield sufficient S/N by conventional fast Fourier transform methods to recover meaningful two dimensional ESE contours from experiments of reasonable duration (ca. 5 h). With linear prediction decomposition and the improved data collection it permits, the whole range is now available to two dimensional ESE.

It has also been possible to use these methods to facilitate accurate projection of two dimensional absorption lineshapes and to suppress certain artifacts that appear in two dimensional ELDOR spectra [46]. For this purpose we have developed a new linear predictive technique, based on linear prediction decomposition [46-48], which models two dimensional time series obtained in COSY type experiments entirely in the time domain, i.e., without Fourier transformation. This new application of complex valued linear prediction facilitates the projection of two dimensional absorption lineshapes as well as the rejection of residual axial peaks and much of the noise.

We wish to acknowledge financial support for this work by NSF Grant No. DMR 8901718 and NIH Grant No. GM25862.

References

[1] Freed, J. H. (1976) Spin Labelling and Applications, Vol I, L. Berliner (ed.), Academic Press, New York, Chapt. 3.
[2] Schneider, D. J. and Freed, J. H. (1989) Lasers, Molecules and Methods, J. O. Hirshfelder, R. E. Wyatt, R. D. Coalson (eds.), John Wiley & Sons, New York, Vol. 73, Adv. Chem. Phys., Chapt. 10.
[3] Budil, D. E., Earle, K. A., Lynch, W. B. and Freed, J. H. (1989) Advanced EPR in Biology and Biochemistry, A. J. Hoff (ed.), Elsevier, Amsterdam, Chapt. 5.
[4] Freed, J. H. (1977) J. chem. Phys., **66**, 4183.
[5] Moro, G. and Nordio, P. L. (1987) J. phys. Chem., **89**, 997.
[6] Abragam, A. (1961) The Principles of Nuclear Magnetism, Oxford University Press, New York.
[7] Gordon, R. G. and Messenger, T. (1972) Electron Spin Relaxation in Liquids, L. T. Muus and P. W. Atkins (eds.), Plenum, New York, Chapt. XIII.
[8] Moro, G. and Freed, J. H. (1981) J. Chem. Phys., **74**, 3757.
[9] Vasavada, K. V., Schneider, D. J. and Freed, J. H. (1981) J. chem. Phys., **86**, 647.
[10] Wilkinson, J. H. (1965) The Algebraic Eigenvalue Problem, Clarendon, Oxford.
[11] Cullum, J. K. and Willoughby, R. A. (1985) Lanczos Algorithms for Large Symmetric Eigenvalue Computations, Birkhauser, Boston.
[12] Golub, G. H. and Van Loan, C. (1983) Matrix Computations, John Hopkins University Press, Baltimore.
[13] Moro, G. and Freed, J. H. (1981) J. chem. Phys., **75**, 3157.
[14] Mori, H. (1965) Progr. Theor. Phys., **34**, 399.
[15] a) Giordano, M., Grigolini, P., Leporini, D. and Martins, P. (1985) Phys. Rev., **A28**, 2474; b) (1985) Adv. chem. Phys., **62**, 321.
[16] Hestenes, M. R. and Stiefel, E. (1952) J. Nat. Bur. Stand., **49**, 409.
[17] Vasavada, K. V. and Freed, J. H. (1989) Computers in Physics, **3**, 61.
[18] Wassam Jr,, W. A. (1985) J. chem. Phys., **82**, 3371; ibid. 3386.
[19] Meirovitch, E. and Freed, J. H. (1984) J. phys. Chem., **88**, 4995.
[20] Hwang, J. S., Rao, K. V. S. and Freed, J. H. (1976) J. phys. Chem., **80**, 1490.
[21] Nayeem, A. and Freed, J. H. (1989) J. phys. Chem., **93**, 6539.

[22] a) McColl, J.R. (1972) Phys. Lett., **38A**, 55; b) McColl, J. R. and Shih, C. S. (1972) Phys. Rev. Lett., 29, 85.
[23] Lin, W. J. and Freed, J. H. (unpublished results).
[24] Cotter, M. (1979) The Molecular Physics of Liquid Crystals, Chapt 8, G. R. Luckhurst, G. W. Gray (eds). Academic Press, New York.
[25] Meirovitch, E., Igner, D., Igner, E., Moro, G., Freed, J. H. (1982) J. chem. Phys., **77**, 3915.
[26] Meirovitch, E. and Freed, J. H. (1980) J. phys. Chem., **84**, 2459.
[27] Rao, K. V. S., Polnaszek, C. F. and Freed, J. H. (1977) J. phys. Chem., **81**, 449.
[28] Lin, W. J. and Freed, J. H. (1979) J. phys. Chem., **83**, 379.
[29] Gorcester, J., Millhauser, G. L. and Freed, J. H. (1989) Advanced EPR in Biology and Biochemistry, A. J. Hoff (ed.), Elsevier, Amsterdam, Chapt. 3.
[30] Luckhurst, G. R., Smith, K. J. and Timimi, B. A. (1980) Molec. Crystals liq. Crystals Lett., **56**, 315.
[31] Kortran, A. R., Kanel, H. V., Birgeneau, R. J. and Litster, J. D. (1981) Phys. Rev. Lett., **67**, 1206.
[32] Bouchet, F. R. and Cladis, P. E. (1980) Molec. Crystals liq., **64**, 81.
[33] Tanaka, H. and Freed, J. H. (1984) J. phys. Chem., **88**, 6633.
[34] McConnell, H. M. (1976) Spin Labelling and Applications, Vol I, L. Berliner, (ed.), Academic Press, New York, Chapt. 13.
[35] Kawato, S., Kinoshita Jr., K. and Ikegami, A. (1978) Biochemistry, **23**, 5026.
[36] Shin, Y. K. and Freed, J. H. (1989) Biophys. J., **55**, 537.
[37] Kar, L., Ney-Igner, E. and Freed, J. H. (1985) Biophys. J., **48**, 569.
[38] Chapman, D., Gomez-Fernandez, J. C. and Goni, F. M. (1979) FEBS Lett., **98**, 211.
[39] Tanaka, H. and Freed, J. H. (1985) J. phys. Chem., **89**, 350.
[40] Jahnig, F. (1981) Molec. Crystals liq. Crystals, **61**, 157.
[41] Millhauser, G. and Freed, J. H. (1984) J. chem. Phys., **81**, 37.
[42] Kar, L., Millhauser, G. L. and Freed, J. H. (1984) J. phys. Chem., **88**, 3951.
[43] Press, W. H., Flannery, B. P., Teukolsky, S. A. and Vetterling, W. T. (1986) Numerical Recipes: The Art of Scientific Computing, Cambridge University Press, New York.
[44] Ge, M. T., Crepeau, R. H. and Freed, J. H. (unpublished results).
[45] Millhauser, G. and Freed, J. H. (1986) J. chem. Phys., **85**, 63.
[46] Gorcester, J. and Freed, J. H. (1988) J. Mag. Res., **78**, 291.
[47] Patyal, B. R., Crepeau, R. H., Gamliel, D. and Freed, J. H. (1990) Chem. Phys. Lett., **175**, 445.
[48] Patyal, B. R., Crepeau, R. H., Gamliel, D. and Freed, J. H. (1990) Chem. Phys. Lett., **175**, 453.